



HAL
open science

Fast quenching of metastable O₂ (a 1Δg) and O₂ (b 1Σg+) molecules by O(3P) atoms at high temperature

Andrey Vladimirovich Volynets, Dmitry Lopaev, T Rakhimova, O Proshina,
Alexander Chukalovsky, Jean-Paul Booth

► To cite this version:

Andrey Vladimirovich Volynets, Dmitry Lopaev, T Rakhimova, O Proshina, Alexander Chukalovsky, et al.. Fast quenching of metastable O₂ (a 1Δg) and O₂ (b 1Σg+) molecules by O(3P) atoms at high temperature. Plasma Sources Science and Technology, 2020, 10.1088/1361-6595/abbf92 . hal-02966916

HAL Id: hal-02966916

<https://hal.science/hal-02966916>

Submitted on 14 Oct 2020

HAL is a multi-disciplinary open access archive for the deposit and dissemination of scientific research documents, whether they are published or not. The documents may come from teaching and research institutions in France or abroad, or from public or private research centers.

L'archive ouverte pluridisciplinaire **HAL**, est destinée au dépôt et à la diffusion de documents scientifiques de niveau recherche, publiés ou non, émanant des établissements d'enseignement et de recherche français ou étrangers, des laboratoires publics ou privés.

ACCEPTED MANUSCRIPT

Fast quenching of metastable $O_2(a^1\Delta_g)$ and $O_2(b^1\Sigma_g^+)$ molecules by $O(^3P)$ atoms at high temperature

To cite this article before publication: Andrey Vladimirovich Volynets *et al* 2020 *Plasma Sources Sci. Technol.* in press
<https://doi.org/10.1088/1361-6595/abbf92>

Manuscript version: Accepted Manuscript

Accepted Manuscript is "the version of the article accepted for publication including all changes made as a result of the peer review process, and which may also include the addition to the article by IOP Publishing of a header, an article ID, a cover sheet and/or an 'Accepted Manuscript' watermark, but excluding any other editing, typesetting or other changes made by IOP Publishing and/or its licensors"

This Accepted Manuscript is © 2020 IOP Publishing Ltd.

During the embargo period (the 12 month period from the publication of the Version of Record of this article), the Accepted Manuscript is fully protected by copyright and cannot be reused or reposted elsewhere.

As the Version of Record of this article is going to be / has been published on a subscription basis, this Accepted Manuscript is available for reuse under a CC BY-NC-ND 3.0 licence after the 12 month embargo period.

After the embargo period, everyone is permitted to use copy and redistribute this article for non-commercial purposes only, provided that they adhere to all the terms of the licence <https://creativecommons.org/licenses/by-nc-nd/3.0>

Although reasonable endeavours have been taken to obtain all necessary permissions from third parties to include their copyrighted content within this article, their full citation and copyright line may not be present in this Accepted Manuscript version. Before using any content from this article, please refer to the Version of Record on IOPscience once published for full citation and copyright details, as permissions will likely be required. All third party content is fully copyright protected, unless specifically stated otherwise in the figure caption in the Version of Record.

View the [article online](#) for updates and enhancements.

Fast quenching of metastable $O_2(a^1\Delta_g)$ and $O_2(b^1\Sigma_g^+)$ molecules by $O(^3P)$ atoms at high temperature

A.V. Volynets¹, D.V. Lopaev¹, T.V. Rakhimova¹, O.V. Proshina¹, A.A. Chukalovsky¹, J.P. Booth²

¹*Skobeltsyn Institute of Nuclear Physics, Lomonosov Moscow State University, Russian Federation*

²*Laboratoire de Physique des Plasmas, CNRS, Ecole Polytechnique, UPMC Univ Paris 06, Univ Paris-Sud, France*

Abstract

Oxygen molecules in the lowest metastable state, $O_2(a^1\Delta_g)$, play an important role in oxygen plasmas due to their high reactivity and significant concentrations. The accumulation of high densities of $O_2(a^1\Delta_g)$ occurs due to its low quenching rate. This paper demonstrates the existence, at high gas temperatures (700-1700K), of fast quenching of $O_2(a^1\Delta_g)$ by $O(^3P)$ atoms, a process that has not been considered in previous models. Experiments were carried out at oxygen pressures of 10-100Torr in an 81MHz CCP discharge in a quartz tube with external electrodes. This setup provides high absorbed power density, leading to both high gas temperatures and significant $O(^3P)$ densities. We observe that the $O_2(a^1\Delta_g)$ density is significantly limited at high gas temperatures by rapid quenching by atomic oxygen. The results were interpreted using a self-consistent 1D discharge model. The observations can only be explained by the inclusion of a rapid quenching reaction: $O_2(a^1\Delta_g) + O(^3P) \rightarrow O_2(X^3\Sigma_g^-) + O(^3P)$, with an activation energy in the range of 0.54-0.69eV. The rate constant was determined over a wide range of discharge conditions ($P = 20-100$ Torr and $T_g = 800-1700$ K), giving values between $3 \cdot 10^{-11} \times \exp(-8000/T)$ cm³/s to $1.5 \cdot 10^{-11} \times \exp(-6300/T)$ cm³/s. A possible mechanism for this process is discussed. Measurements of the density of metastable $O_2(b^1\Sigma_g^+)$ molecules also indicated the existence of quenching by atomic oxygen, with a somewhat lower activation energy of ~0.32 eV. The variations of the measured $[O_2(b^1\Sigma_g^+)]/N$ mole-fraction could be fitted by the model using a rate constant - $2 \cdot 10^{-11} \cdot \exp(-3700/T)$ cm³/s for this process. These quenching processes of metastable $O_2(a^1\Delta_g)$ and $O_2(b^1\Sigma_g^+)$ molecules by oxygen atoms are important for oxygen plasmas and could have a significant impact on the kinetics of oxygen-containing mixtures at higher gas temperatures, for example in plasma-assisted combustion or in high-pressure plasma processing reactors.

1. Introduction

Oxygen plasmas have been the subject of much research. It attracts attention due to their high chemical reactivity, due to high concentrations of active particles including oxygen atoms and electronically excited metastable molecules, notably singlet oxygen, $O_2(a^1\Delta_g)$. These reactive species are essential in many technological plasma processes [1], [2], lasers [3]–[8] and combustion [9]–[13].

The dissociation degree of oxygen molecules in plasmas can be very high ($> 20\%$ [14]), while $O_2(a^1\Delta_g)$ yield can reach $\sim 15\%$ [15]–[17]. Significant amounts of these species define not only the reactivity of O_2 plasmas but also strongly influence the plasma itself. For example, the destruction of negative ions through detachment processes with $O(^3P)$ and $O_2(a^1\Delta_g)$ controls the electronegativity of O_2 plasmas, and thereby influences other parameters such as the electric field, electron energy distribution function (EEDF) etc. [18]–[21]. Therefore, it is very important to understand and model the kinetics of atomic and singlet oxygen. The generally accepted kinetic scheme for processes involving $O(^3P)$ and $O_2(a^1\Delta_g)$ with neutral species has been well established [3], [4], [22]–[27]. However, the mechanisms of $O_2(a^1\Delta_g)$ production and quenching via reactions involving transitory species requires further detailed investigation. While it is commonly accepted that volume reactions are known relatively well, surface processes are less well characterized, and can have a strong effect at lower pressures. At higher pressures volume processes become dominant. While reactions between stable species are generally well known, processes with radicals have been less studied. Even when rate constant data is available, it is often scattered over a wide range.

Volume quenching of $O_2(a^1\Delta_g)$ in reactions with oxygen atoms is one of most important processes determining its concentration. This process has been observed in different oxygen-containing plasmas [19], [22], [23], [28], [29] and photolysis experiments [30]. In [8], [28], [31] the quenching of $O_2(a^1\Delta_g)$ in a plasma afterglow was explained by reactions with vibrationally excited ozone molecules, which are produced by the initial stage in three-body recombination with O_2 [32]. In [3], [23], [33] the three-body recombination of $O(^3P)$ atoms with $O_2(a^1\Delta_g)$ was invoked to explain the observed fast loss of $O_2(a^1\Delta_g)$ at gas temperature $T_g < 700K$. This three-body reaction was used as “gross”-reaction to describe a two-step mechanism of $O_2(a^1\Delta_g)$ loss due to stabilization of the excited compound state of O_3 to the repulsing part of the bounded electron states. In all these studies mechanisms are invoked to explain observed increases in the quenching rate with pressure, but the effect of the gas temperature was ignored. Nevertheless, these studies demonstrated that fast quenching of $O_2(a^1\Delta_g)$ by $O(^3P)$ atoms has a significant effect on the $O_2(a^1\Delta_g)$ concentration and whole plasma behaviour.

This paper presents a detailed experimental study of $O_2(a^1\Delta_g)$ quenching by $O(^3P)$ atoms. For this goal we studied a dense oxygen plasma at relatively high gas pressure (10-100Torr) in a quartz tube, conditions which minimize the surface influence on $O_2(a^1\Delta_g)$ quenching. The plasma was generated by a 81MHz CCP (capacitively coupled plasma) discharge with external electrodes to provide high absorbed power, and thereby high density of $O(^3P)$ atoms at gas temperature up to $\sim 1700K$. These specially created conditions allowed us to observe directly very fast $O_2(a^1\Delta_g)$ quenching by oxygen atoms. Detailed comparison of the experimental data to a 1D self-consistent discharge model enabled different possible mechanisms to be investigated, and the determination of rate constants for the corresponding quenching process. Additionally, the behavior of O_2 molecules in the second metastable state, $b^1\Sigma_g^+$, was also studied. These results showed that an analogous fast quenching reaction by $O(^3P)$ atoms also exists for $O_2(b^1\Sigma_g^+)$, but with a lower activation energy.

The paper is organized as follows. Details of the experiment and some important results are presented in Section 2. The discharge model and kinetics scheme are described in Section 3. Section 4 is devoted to the model-based analysis of the data and discussion of the results. At last, a conclusion is given in Section 5.

2. Experiment

The experimental setup is shown in Figure 1, and has been presented previously in detail. Here we will present briefly only the features relevant to this study. The capacitively-coupled plasma (CCP) in O_2 gas was generated in a quartz tube (wall thickness - 2mm) of length 200 mm and inner diameter 10 mm with external electrodes running the whole length of the tube. The electrodes were driven by a 81 MHz generator at power 50-500 W, producing a quasi-uniform plasma column along the tube over a wide pressure range (10 – 100 Torr). Significantly, there are no the arms without plasma in the tube ends where ozone can accumulate. To avoid tube heating and to keep the surface conditions stable, the electrodes were cooled by internally-flowing water, with soft carbon inserts providing good thermal contact between the tube and the electrodes. A matching network allowed the reflected rf power to be minimized, and did not exceed 1-2 W, but some rf power was dissipated in the matching network. Since the discharge is close to symmetric, both the rf voltage and rf current waveforms were close to sinusoidal. Therefore the rf power consumed by the plasma can be estimated from the measured effective values of the rf voltage and rf current and their phase shift, measured directly at the electrodes using corresponding probes and a phase-vector meter.

The rf generator could operate in both continuous and pulsed modes, with variable power modulation depth. This discharge configuration provides high specific power input; along with the high gas pressure this leads to high gas temperatures. This also produces high O_2 dissociation degree, since the loss probability of atomic oxygen on quartz is rather small ($\sim 10^{-3}$), and no metal parts are present inside the tube.

Pure oxygen (99.99 %) was used for most measurements. 2.5% of Kr was added to oxygen in some cases for actinometric measurements. This small addition of krypton is not expected to strongly influence the discharge parameters due to the higher ionization potential for Kr compared to O₂. The small O₂ flow rate of 20 sccm provided gas residence times longer than the lifetime of all active species produced in the discharge.

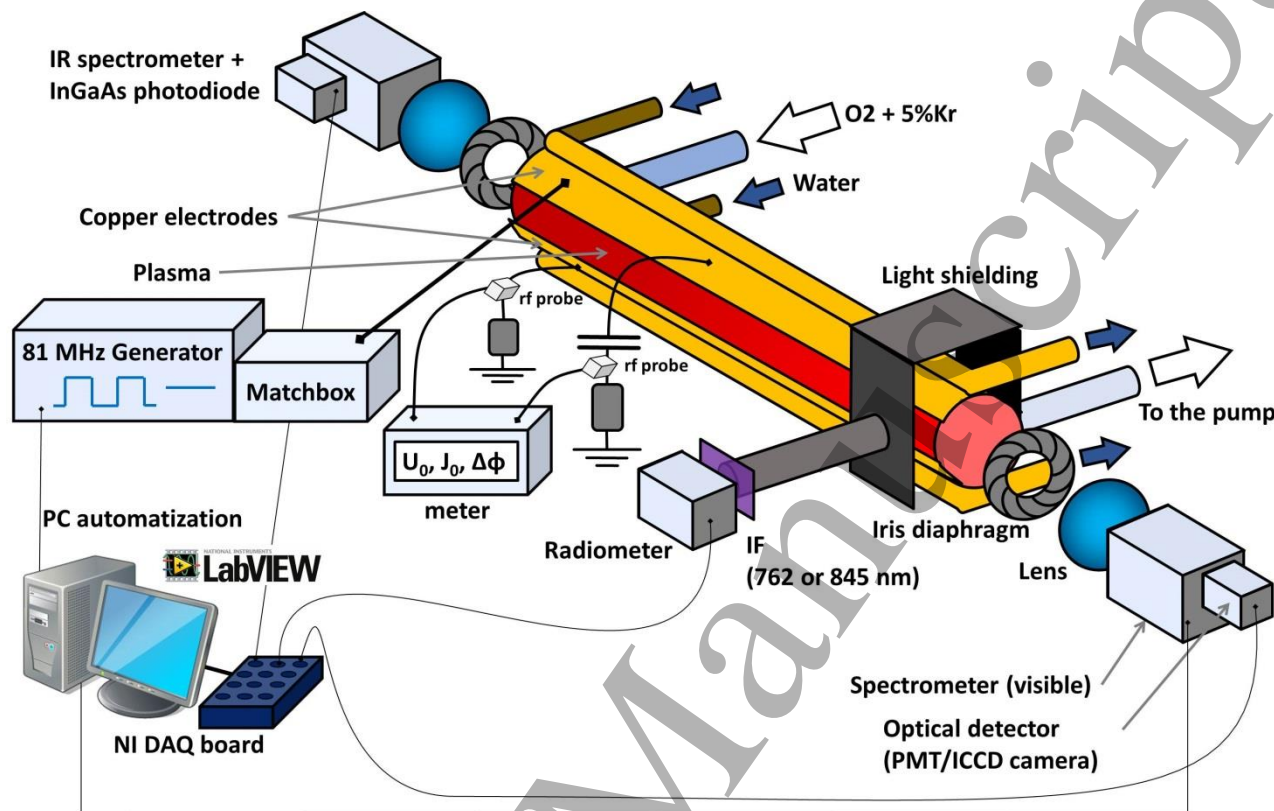


Figure 1. Experimental setup (see text for details).

Optical emission spectroscopy was used the main tool in this research. Light from the discharge was observed through optical quality quartz windows fused to both ends of the quartz tube. The emitted light was passed through a variable iris diaphragm and focused onto the entrance slit of a visible or a near IR monochromator, fitted with appropriate detectors: an ICCD matrix or PMT (for visible spectral range) and an InGaAs photodiode (for the near IR spectral range).

Programs created in the NI LabVIEW environment and a NI DAQ device were used to control the discharge, record the results of the optical diagnostics, and process the obtained data.

2.1 $O_2(b^1\Sigma_g^+)$ and T_g measurements

The gas temperature T_g was determined from the observed A-band $O_2(b^1\Sigma_g^+, v=0) \rightarrow O_2(X^3\Sigma_g^-, v=0)$ emission by fitting to spectral simulations as described previously [14], [34], [35]. The $O_2(b^1\Sigma_g^+)$ emission was collected through the quartz window in the end of the tube. Iris diaphragm and condenser allowed to select area of the discharge, from which the emission were collected [34]. The

spectral resolution was adequate to resolve the rotational structure of the P-branch. This technique provides an accuracy of T_g determination about $\pm 20\text{K}$. The spatial resolution was not able to fully resolve the spatial profile of T_g , but was enough to isolate the emission from axial region (with diameter $\sim 2\text{-}3\text{mm}$). Therefore we were able to determine both the temperature near the axis - $T_{g\text{-axis}}$, and the temperature averaged over the tube diameter - $T_{g\text{-aver}}$.

The $\text{O}_2(b^1\Sigma_g^+)$ density averaged over the tube diameter (in accordance with that discharge emission selected by the spectrometer slit, see Figure 1) was estimated from the integral of the A-band intensity after subtracting the background emission, and performing an absolute intensity calibration. The absolute calibration was based on direct measurement of the $\text{O}_2(b^1\Sigma_g^+, v=0) \rightarrow \text{O}_2(X^3\Sigma_g^-, v=0)$ radiation power from a small part of the tube limited by dark screens, as shown in Figure 1. The emission intensity was determined using an absolutely-calibrated radiometer, fitted with an interference filter (765 nm, bandwidth ~ 10 nm FWHM). The absolute measurements were carried out at the lowest powers and at pressures below 40 Torr, in order to minimize background emission. The $\text{O}_2(b^1\Sigma_g^+)$ density was then obtained from the radiometer measurements as follows:

$$[\text{O}_2(b^1\Sigma_g^+)] \approx \frac{4\pi L^2 \cdot P_{rad} \cdot \xi}{h\nu \cdot A \cdot \eta_{IF} \cdot V},$$

where P_{rad} is power measured by radiometer, $h\nu/e = 1.62$ eV, $A = 8.34 \cdot 10^{-2}$ [36] is the Einstein coefficient, L is distance from tube axis to the radiometer detector head ($L \gg R_{tube}$), η_{IF} is convolution of measured $\text{O}_2(b^1\Sigma_g^+, v=0) \rightarrow \text{O}_2(X^3\Sigma_g^-, v=0)$ spectrum with the transmission of the interference filter at 765 nm, V is emitting volume and ξ is correction factor accounting for contributions of $\text{O}_2(b^1\Sigma_g^+)$ and background emissions into the radiometer signal (the correction factor ξ was estimated from measured discharge spectra in the range of $\text{O}_2(b^1\Sigma_g^+, v=0) \rightarrow \text{O}_2(X^3\Sigma_g^-, v=0)$ band). The measurements were performed at two different distances (14 and 24 cm) of the radiometer head, in order to estimate the possible uncertainty of the absolute calibration.

2.2 $\text{O}(^3P)$ measurements

The optical emission actinometry technique was used to estimate the mole fraction of atomic oxygen. The applicability of this well-known method for the given conditions has been previously discussed in detail [34]. A specificity in this case is that two actinometer gases, Ar and Kr, were used simultaneously. 2.5% Kr and 2.5% Ar were added to O_2 . This percentage was assumed not to influence the plasma parameters. The two actinometer gases were used because of the high pressures in this study. Under the conditions studied, the effective electric field in the plasma bulk, and the corresponding electron temperature, are quite small. This increases the uncertainty in estimating actinometric coefficients, i.e. the coefficient relating the emission intensity ratios to the atom densities. The gap between the excitation energies of the observed emitting levels of oxygen and krypton is smaller than characteristic electron temperature T_e ($\sim 1.8\text{-}2.2$ eV), whereas the gap

between those for Ar and Kr is higher. Therefore the ratio of the Ar to Kr intensities is sensitive to T_e changes, and thereby gives additional control for O atom actinometric coefficients.

The following atomic lines were used: $O(^5P) \rightarrow O(^5S)$ (777 nm), $Kr(2p_5) \rightarrow Kr(1s_4)$ (758 nm), $Kr(2p_9) \rightarrow Kr(1s_5)$ (811 nm) and $Ar(2p_1) \rightarrow Ar(1s_2)$ (750 nm). It is worth noting that in the considered pressure range (10 – 100 Torr) collisional quenching of emitting states prevails over radiative decay:

$$\frac{[O(^3P)]}{N} \approx C_{Kr}^O \frac{S_{\lambda}^{Kr}}{S_{\lambda}^O} \frac{I_O}{I_{Kr}} \frac{[Kr]}{N} \quad (1)$$

while dissociation excitation of O_2 could be neglected because of low T_e . N is the total gas density. C_{Kr}^O is the so-called actinometrical coefficient:

$$C_{Kr}^O = \frac{\sum_j A_{ij}^O + k_q^O [O_2]}{\sum_m A_{nm}^{Kr} + k_q^{Kr} [O_2]} \frac{A_{nm}^{Kr} k_e^{Kr}}{A_{ij}^O k_e^O} \approx \frac{k_q^O}{k_q^{Kr}} \frac{A_{nm}^{Kr} k_e^{Kr}}{A_{ij}^O k_e^O} \quad (2)$$

where A_{ij} is Einstein coefficients of radiative transition from the i -th upper (emitting) state to j -th lower state, k_q^O and k_q^{Kr} are quenching rate constants of the upper state of O and Kr atoms in collision processes with neutral particles (O_2), S_{λ}^O and S_{λ}^{Kr} are sensitivities of spectroscopic system at the wavelength of O and Kr atoms. Finally, k_e^O and k_e^{Kr} are excitation rate constants by electron impact from ground to the upper emitting state of O and Kr atoms. The excitation rate constants were calculated by convolution of the corresponding excitation cross section with EEDF. The value of the excitation rate constant is rather sensitive to the shape EEDF as well as to small changes of the effective electron temperature, T_e . However, the *ratio* between the excitation rate constants is less sensitive, and if the considered energy levels are close the ratio will vary only little. This is the case for the chosen O and Kr states. Thus, the ratio between the excitation rate constants were calculated in advance using the experimentally estimated E/N_{eff} and the available excitation cross sections [37]–[40]. Effective values of the reduced electric field, E/N_{eff} , were estimated from the Kr to Ar line emission ratio with 2.5% of Ar and Kr added to O_2 [34]. Since in this case of O/Kr the shape of the EEDF has little influence on the actinometric coefficient, the BOLSIG+ software [41] was used to calculate the EEDF as a function of E/N_{eff} . The Einstein coefficients were taken from the NIST database [42].

Precise values of quenching rate constants are very important for the correct determination of $O(^3P)$ atom density at high pressure. Unfortunately, these values are not well-known, and furthermore may depend upon the gas temperature. However, any temperature effect is partly compensated due to the fact that the actinometric coefficient includes the *ratio* between the quenching rate constants. All the above questions have been considered in detail previously [34].

Overall, the accuracy of the oxygen atom density determination depends on the uncertainties of both $[O(^3P)]/N$ and T_g . The uncertainties in $[O(^3P)]/N$ can be quite high due to all the uncertainties in the parameters used in equations (1) and (2), but above all due to the uncertainties

in the cross sections of the quenching rate constants. Following the data from [34] and making a comparison with model (see below), we estimate the uncertainties of the absolute measurements of $[O(^3P)]/N$ to be within $\pm 30\%$.

2.3 $O_2(a^1\Delta_g)$ measurements

Similar to $O_2(b^1\Sigma_g^+)$, the $O_2(a^1\Delta_g)$ density was measured by OES. The discharge emission spectrum around 1270nm of the $O_2(a^1\Delta_g, v=0) \rightarrow O_2(X^3\Sigma_g^-, v=0)$ band was detected using the IR monochromator with InGaAs detector. The detector signal after trans-impedance amplifier ($2 \cdot 10^{10}$ V/A) was fed to the DAQ card. A typical discharge spectrum is shown in Figure 2. The spectral resolution (~ 2.5 nm) was adequate to clearly observe the $O_2(a^1\Delta_g)$ emission band. However compared with $O_2(b^1\Sigma_g^+)$, the level of background emission was higher. This is due to weak atomic oxygen lines occurring on the wings of the $O_2(a^1\Delta_g, v=0) \rightarrow O_2(X^3\Sigma_g^-, v=0)$ band, as well as chemiluminescence from excited NO_2^* molecules (present due to some nitrogen in the tube). The small amount of nitrogen ($< 0.05\%$) was in the tube due to small leaks in gas and vacuum systems (flow leak was less than 0.01 sccm, which is typical for most plasma reactors using seals for glass tubes and windows). The quantity of nitrogen, and correspondingly NO_2 , is very small. However the NO_2 emission is very bright, since it is an allowed transition, and therefore can always be even seen next to the very weak $O_2(a^1\Delta_g)$ emission. Since the background emission consisted principally of this wideband (almost continuous) contribution in the range of the $O_2(a^1\Delta_g, v=0) \rightarrow O_2(X^3\Sigma_g^-, v=0)$ band, the background emission was estimated as shown in Figure 2. The background was then subtracted to give the value of the $O_2(a^1\Delta_g)$ emission intensity.

The $O_2(a^1\Delta_g)$ density averaged over the tube diameter was obtained from the absolutely-calibrated the emission intensity integrated over the $O_2(a^1\Delta_g, v=0) \rightarrow O_2(X^3\Sigma_g^-, v=0)$ band. The calibration was made by measuring the $O_2(a^1\Delta_g)$ radiation power using the same radiometer as in case of the $O_2(b^1\Sigma_g^+)$ calibration. Since the radiometer uses a Si-based detector which is not sensitive to IR $O_2(a^1\Delta_g)$ radiation, direct measurement of $O_2(a^1\Delta_g)$ radiation power was not possible. Therefore the absolute calibration of $O_2(a^1\Delta_g)$ emission measurements was carried out by measuring the radiation power from the oxygen atom 845 nm line using the radiometer, and simultaneously by the monochromator + InGaAs detector system. An interference filter (845 nm, bandwidth ~ 10 nm FWHM) was used on the radiometer detector head to select the O845 nm line from the discharge emission. The $O_2(a^1\Delta_g)$ density was then determined by:

$$[O_2(a^1\Delta_g)] = \frac{\int I_{O2(a)} d\lambda}{\int I_{O845} d\lambda} \cdot \frac{\eta_{sp845}}{\eta_{sp1270}} \cdot \frac{4\pi L^2 \cdot P_{O845}}{h\nu \cdot A \cdot V \cdot \eta_{IF845}},$$

where P_{O845} is O845 nm line power measured by radiometer, L is a distance to the radiometer detector head from tube axis (while $L \gg R_{\text{tube}}$), η_{IF845} is the transparency of interference filter (60 %) at 845 nm, $h\nu/e = 0.98$ eV, $A = 2.256 \cdot 10^{-4}$ is the Einstein coefficient for the transition, V is the emitting volume (the same as in calibration for $O_2(b^1\Sigma_g^+)$), η_{sp845} and η_{sp1270} are products of the InGaAs sensitivity and the reflectivity of the mirrors and grating of monochromator for 845 and 1270 nm respectively, $\int I_{O845} d\lambda$ and $\int I_{O2(a)} d\lambda$ are the spectrally-integrated intensities of the O atom 845 nm line and the $O_2(a^1\Delta_g)$ 1270 nm band measured by monochromator + InGaAs detector system. The accuracy of the absolute $O_2(a^1\Delta_g)$ density is estimated to be within $\pm 20\%$.

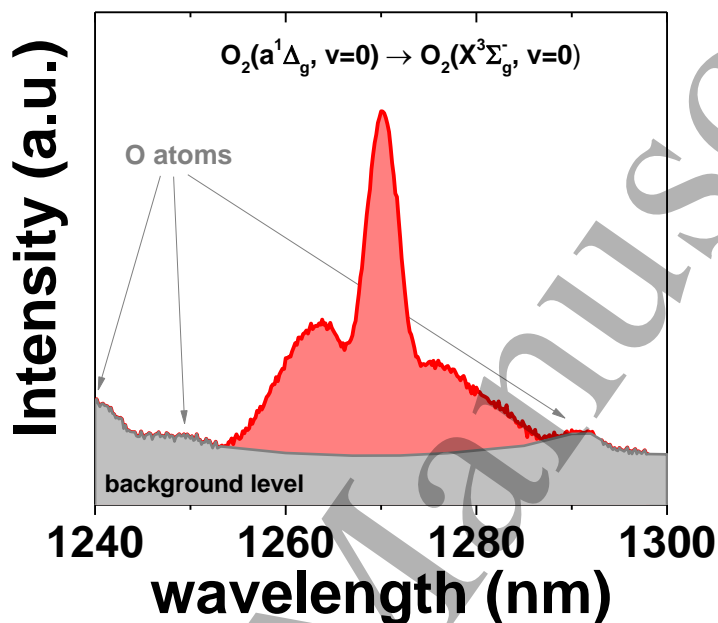


Figure 2. Example of an measured emission spectrum around 1270 nm at 20 Torr and 41W of input rf power. The estimated level of background emission is shown in grey, while the emission of the $O_2(a^1\Delta_g, v=0) \rightarrow O_2(X^3\Sigma_g^-, v=0)$ band is shown in red. The weak O atom lines in accordance with NIST database are marked by arrows.

Firstly, we investigated the $O_2(a^1\Delta_g)$ kinetics during full discharge modulation. This was principally to characterize processes with $O_2(a^1\Delta_g)$ molecules in afterglow, where the role of oxygen atoms and ozone can be essential. The temporal behavior of the discharge emission at wavelengths corresponding to $O_2(a^1\Delta_g)$ peak emission at 1270 nm and background emission at 1252 nm was recorded. An example is presented in Figure 3a. In the discharge afterglow only the $O_2(a^1\Delta_g)$ emission is observed. The dynamics of the $O_2(a^1\Delta_g)$ density at 30 Torr and different input rf powers is shown in Figure 3b.

After turning on discharge, the $O_2(a^1\Delta_g)$ density increases quickly during the first few tens ms, then starts to saturate. At low input rf power the saturation occurs later, indicating a lower rate of $O_2(a^1\Delta_g)$ quenching. With increasing rf power the initial rate of increase in the $O_2(a^1\Delta_g)$ density

increases. However, saturation occurs in a shorter time at high power, and at the highest powers the density of $O_2(a^1\Delta_g)$ actually decreases at longer times. It should be noted that the gas temperature (and the corresponding gas density) stabilizes in ~ 3 ms. Indirectly, this is confirmed by the sharp jump up of the $O_2(a^1\Delta_g)$ density after discharge extinction and the corresponding gas cooling (see below). This time approximately corresponds to characteristic time for thermal conduction in the radial direction. Thus, this behavior of the $O_2(a^1\Delta_g)$ density over hundreds of milliseconds can only be explained by the presence of significant collisional quenching of $O_2(a^1\Delta_g)$ in the discharge, caused by a species whose density grows with increasing input rf power. The only possible candidates for this quenching are $O(^3P)$ atoms and O_3 molecules. However, measurements have shown that the O_3 density is very low in the active discharge [34]. Moreover, nearly all of the ozone is found close to the cold walls, and is essentially absent in the plasma region due to fast decomposition at high gas temperature. The ozone concentration is too low (by several orders of magnitude) to cause the observed rate of $O_2(a^1\Delta_g)$ quenching. Since the electron density stabilizes quickly (in a few hundred of microseconds), $O(^3P)$ atoms are the only quenching species present in high enough concentration to explain the $O_2(a^1\Delta_g)$ loss during discharge pulse.

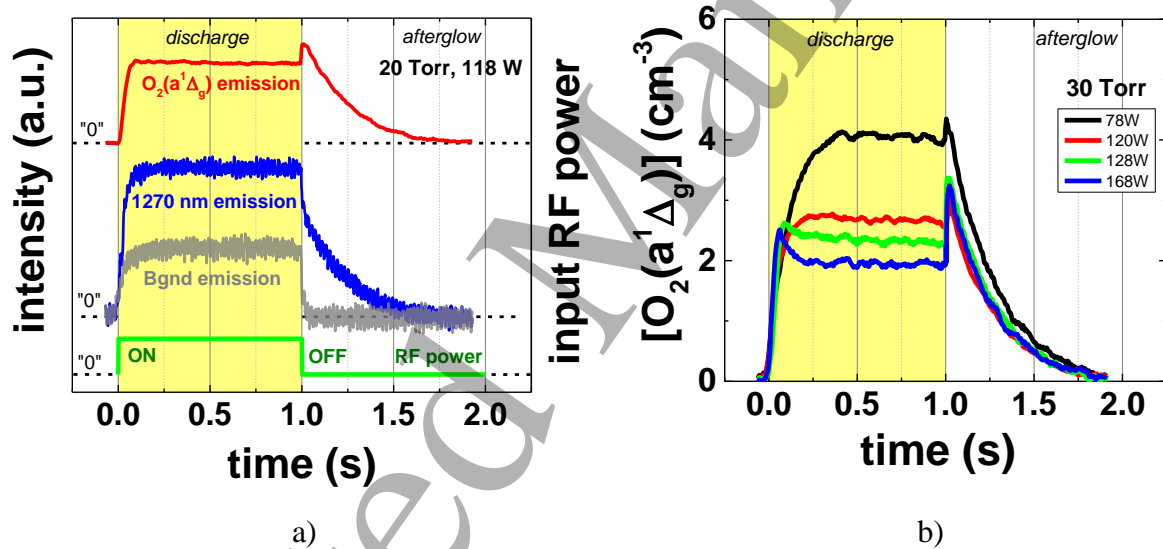
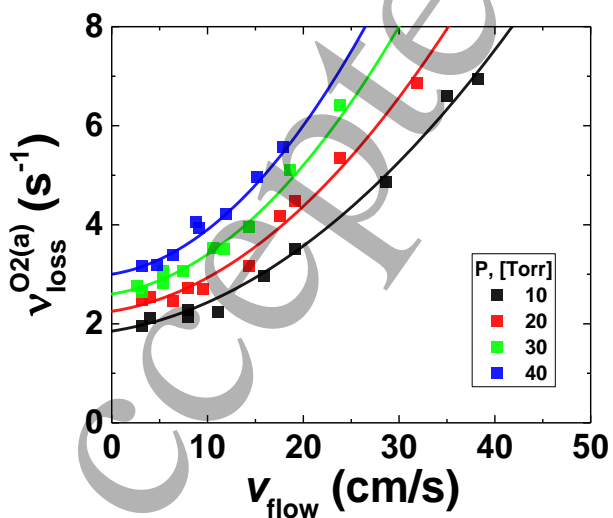


Figure 3. a) Examples of the dynamics of the discharge emission: at 1270nm ($O_2(a^1\Delta_g)$ + background) (blue), Background at 1252nm background (grey) and the difference (= $O_2(a^1\Delta_g)$ emission) (red) during full discharge modulation at 20 Torr. The dashed lines correspond to zero, “0”, for each signal. b) Dynamics of $O_2(a^1\Delta_g)$ density during full modulation at 30 Torr and different input rf powers.

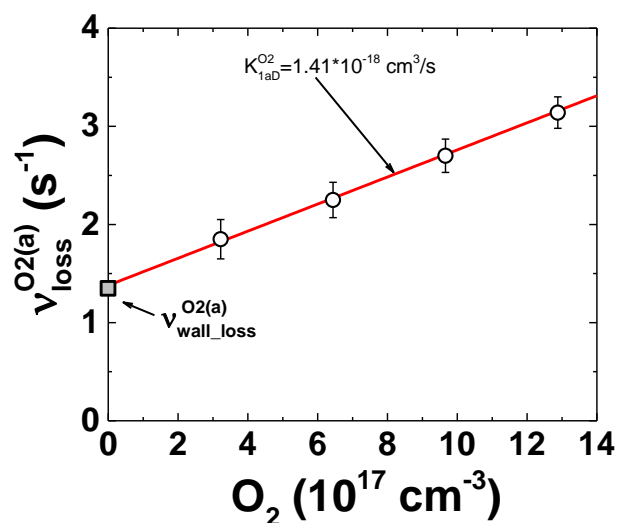
Immediately after turning off the discharge, a fast (during ~ 3 ms) rise of the $O_2(a^1\Delta_g)$ density is observed, which can be attributed to gas cooling and convection towards the discharge center. As seen, this jump becomes more marked at higher input rf power, due to the higher gas temperature. Subsequently, the gas temperature approaches the wall temperature, and the $O_2(a^1\Delta_g)$ density in the

afterglow follows an exponential decay $\sim \exp(-\nu_{loss}^{O_2(a)} t)$ with a constant loss frequency $\nu_{loss}^{O_2(a)}$ which is almost independent of the rf power. This shows that the discharge does not create any significant density of stable species which can quench $O_2(a^1\Delta_g)$ (O_3 for instance).

Figure 4a shows the variation of the $O_2(a^1\Delta_g)$ loss frequency in the afterglow, $\nu_{loss}^{O_2(a)}$, as a function of gas flow velocity at different pressures. It progressively increases with flow velocity at all pressures, demonstrating the effect of the gas residence time on $O_2(a^1\Delta_g)$ loss. The extrapolated values for zero flow velocity correspond to the $O_2(a^1\Delta_g)$ loss frequency due to gas-phase processes at each pressure. These extrapolated values are plotted as a function of the O_2 density in Figure 4b. The O_2 density can be calculated simply from the gas pressure, since gas temperature has relaxed to equilibrium with the wall $T_g \approx 285K$. The pressure dependence can be approximated by a linear function, with an intersection at zero O_2 density corresponding to the $O_2(a^1\Delta_g)$ loss frequency due to quenching on the tube wall. From this, one can determine a $O_2(a^1\Delta_g)$ surface loss probability, $\gamma_\Delta \approx 4 \cdot 10^{-5}$. This is in good agreement with other measurements of γ_Δ on quartz surfaces outside plasma [43]. The slope of the linear dependence provides a rate constant for the quenching of $O_2(a^1\Delta_g)$ by O_2 molecules of $k_q^{O_2} \approx 1.4 \cdot 10^{-18} \text{ cm}^3/\text{s}$ at 285K. This $k_q^{O_2}$ value also agrees very well with data in the literature [43]–[46]. This shows that neither oxygen atoms or ozone cause significant $O_2(a^1\Delta_g)$ quenching in the afterglow. Indeed, as was shown in [34], the characteristic time for $O(^3P)$ atom recombination (both volume and surface) is short, $\sim 2\text{-}3 \text{ ms}$. Thus, the majority of the $O(^3P)$ atoms are able to recombine during the initial high temperatures at the beginning of the afterglow. Furthermore, any O_3 molecules created in this period will also be destroyed by fast reactions at these high temperatures. We tried to measure the dynamics of O_3 density in the discharge afterglow using UV absorption [34]. This showed that the ozone density in the afterglow is low ($< 5 \cdot 10^{13} \text{ cm}^{-3}$) and comes mostly from O_3 diffusion from a thin layer near the cold wall where ozone accumulates during the discharge.



a)



b)

Figure 4. a) $O_2(a^1\Delta_g)$ loss frequency in the afterglow as function of gas flow velocity at different pressures. The symbols are experimental data, and the lines are fits. b) Loss frequency of $O_2(a^1\Delta_g)$ at zero gas flow as function of O_2 density ($T_g \approx 285K$). The intersection at zero O_2 density corresponds to the $O_2(a^1\Delta_g)$ loss frequency on the tube wall ($\gamma_\Delta \approx 4 \cdot 10^{-5}$) while the slope of the linear dependence corresponds to the $O_2(a^1\Delta_g)$ quenching rate constant by O_2 molecules: $k_q^{O_2} \approx 1.4 \cdot 10^{-18} \text{ cm}^3/\text{s}$.

During the active discharge period the $O_2(a^1\Delta_g)$ loss frequency is noticeably higher than in the afterglow (for example see the $[O_2(a^1\Delta_g)]$ dynamics in Figure 3 during full modulation of the rf power and the dynamics of the $O_2(a^1\Delta_g)$ mole fraction during partial modulation shown in Figure 9). Therefore the observed fast quenching of $O_2(a^1\Delta_g)$ in the discharge can only be attributed to $O(^3P)$ atoms. Measurements of the $O_2(a^1\Delta_g)$ dynamics during partial modulation of the rf power have shown that the rate of this quenching significantly rises with pressure and input power (i.e. gas temperature) increase. Therefore higher gas temperatures notably speed up the $O_2(a^1\Delta_g)$ quenching by $O(^3P)$ atoms, indicating that this reaction has a significant activation energy barrier. It should be noted that such a reaction has not been proposed prior to this study.

3. Model

The self-consistent 1D model of an rf discharge used here is similar in principle to that presented by Braginskiy et al. [23] and will only be described briefly here. The transport of electrons and positive and negative ions is described by the continuity equations, the drift diffusion approximation is used to calculate charged species fluxes. The discharge is assumed to operate in the so-called rf-discharge α -mode, and therefore secondary electron emission is not included.

The average electron energy, ε_e is deduced from the electron energy balance equation. The electron induced reaction rates, the electron mobility and diffusion coefficients as calculated as functions of ε_e and n_e by solving the local (0D) Boltzmann equation for the EEDF in the two-term approximation [23]. The solution of the 0D Boltzmann equation is a pre-processing step to generate so-called ε_e -based lookup tables (electron related coefficients as functions of ε_e and n_e) that are then used during the plasma simulation. This method can be applied to intermediate pressure plasmas [23], [47], provided that the electron energy balance takes into account non-local effects such as electron thermal conductivity.

The self-consistent electric field is found by solving the Poisson equation. The rf voltage amplitude is adjusted to match the average specific power input calculated from the measured absorbed power and the plasma volume (16cm^3). The calculated specific power input was defined

as the spatially-averaged power dissipated into electrons and ions in the plasma along the whole inter-electrode space of 1 cm.

We decided that this is the most appropriate way to compare our experimental data to the 1D rectangular simulation, given that the geometry of the discharge tube and the profiled electrodes is complex and three-dimensional. At the same time using 1D-simulation is enough for the present task. This is because we consider spatially-homogeneous rf discharge in the α -mode, and validate the spatially-averaged densities of the relevant neutral species - $O(^3P)$, $O_2(a^1\Delta_g)$, $O_2(b^1\Sigma_g^+)$, with the measured data to reveal specific features of volume plasma chemistry such as reactive quenching reactions for $O_2(a^1\Delta_g)$ and $O_2(b^1\Sigma_g^+)$.

The spatial distributions of the neutral components are also calculated by continuity equations. The wall loss probabilities for the active radicals are shown in Table 1. These correspond to the experimentally-estimated values for the quartz tube (except for $O(^1D)$ and O_2^* where O_2^* denotes sum of Herzberg states). It should be noted that for the pressure range under study only heterogeneous quenching of $O(^3P)$ plays a significant role, so the value of γ_O is significant [34], whereas the concentrations of other electronically excited atoms and molecules are determined totally by fast volume reactions (see the next section).

Table 1. Surface loss probabilities for neutral radicals (O_2^* denotes sum of Herzberg states).

Surface Reaction	Loss probability γ (quartz)
$O_2(a^1\Delta_g)$	0.00005
$O_2(b^1\Sigma_g^+)$	0.1
O_2^*	1
$O(^3P)$	0.001
$O(^1D)$	1

The spatial distribution of the gas temperature was found from the solution of the gas thermal energy balance equation. In order to effectively take into account the thermal conductivity and diffusion of neutral species in the perpendicular transverse direction (across the tube toward the tube wall sectors which do not side with electrodes) we increased the thermal conductivity coefficient η and the diffusion coefficient D in the following way:

$$D_{\text{eff}} = c_1 \cdot D, \quad \eta_{\text{eff}} = c_2 \cdot \eta, \quad c_1 = \frac{(L_{\text{cyl}})^{-2}}{(L_{\text{plane}})^{-2}} \approx 2.33 \quad c_2 = 0.8 \cdot c_1 \quad (1)$$

where $L_{\text{cyl}} = (2.4/R)^2$ is the characteristic diffusion length for an endless cylinder of radius R and $L_{\text{plane}} = (\pi/2R)^2$ is the characteristic diffusion length for two endless parallel plates with a distance of

2R between them. The value of c_2 is lower than c_1 by a factor of 0.8 which takes into account the different cooling rates of regions of the tube wall, those sides with metal electrodes having a wall temperature of 300K, compared to the transverse wall that is cooled only by quartz thermal conductivity and outside air convection. It should be noted also that we do not simulate directly the tube wall area and the cooling inside it, therefore the gas temperature near the tube wall T_{g-w} is the boundary condition for the gas temperature equation. T_{g-w} is model parameter since it was measured in [34] with great uncertainty. According to the results of [34], we chose two different values of $T_{g-w} = 400K$ and $T_{g-w} = 300K$ to investigate its influence on the simulation results. This may be valuable not only for the resulting gas temperature distribution inside the tube, but also for the spatial distribution of different neutral species, since many volume reaction rates between neutral species depend on the gas temperature, and the resultant spatial distribution of different neutral species across the tube can be essentially inhomogeneous.

The O_2 plasma reaction mechanism and electron cross section database used were almost the same as that described in [23]. However, at these elevated gas temperatures and pressures, the transformation of energy stored in electronically excited metastables is dependent not only on electronic and heterogeneous processes, but also by processes involving atomic oxygen, the rate constants of which can significantly depend on gas temperature. Therefore, in this section we will make a brief description of the processes included in our updated kinetic scheme, which determine the transformation of electronic excitation in reactions with neutral particles, presented in Table 2. Besides, some possible mechanisms for the reactions of $O_2(a^1\Delta_g)$ and $O_2(b^1\Sigma_g^+)$ with $O(^3P)$ atoms are considered also on the base of the data available in the literature.

Table 2. Neutral kinetics for $O_2(a^1\Delta_g)$ and $O_2(b^1\Sigma_g^+)$ included in updated kinetic scheme [23].

#	Reaction	Rate constant, cm ³ /s, s ⁻¹ , cm ⁶ /s	Reference
(R1)	$O(^1D) + O_2 \rightarrow O_2(X^3\Sigma) + O$	$0.64^{-11} \times \exp(67/T)$	[48], [49]
(R2)	$O(^1D) + O_2 \rightarrow O_2(b^1\Sigma_g^+) + O$	$2.56 \cdot 10^{-11} \times \exp(67/T)$	[48], [49]
(R3)	$O_2(b^1\Sigma_g^+) + O(^3P) \rightarrow O(^1D) + O_2(X^3\Sigma)$	$3.39 \cdot 10^{-11} \times (300/T)^{0.1} \times \exp(-4201/T)$	[50]
(R4)	$O_2(b^1\Sigma_g^+) + O_2 \rightarrow O_2(X^3\Sigma_g^-) + O_2$	$7.4 \cdot 10^{-17} \times T^{0.5} \times \exp(-1104/T)$	[51]
(R5)	$O_2(a^1\Delta_g) + O(^3P) \rightarrow O_2(X^3\Sigma_g^-) + O(^3P)$	$7 \cdot 10^{-16}$	[52]
(R6)	$O_2(b^1\Sigma_g^+) + O(^3P) \rightarrow O_2(a^1\Delta_g) + O(^3P)$	$8 \cdot 10^{-14}$	[53]
(R7)	$O_2(a^1\Delta_g) + O(^3P) \rightarrow O_2(X^3\Sigma_g^-) + O(^3P)$	$1.5 \cdot 10^{-11} \times \exp(-6300/T)$ or $3 \cdot 10^{-11} \times \exp(-8000/T)$	this work, see text

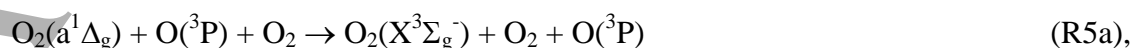
(R8)	$O_2(b^1\Sigma_g^+) + O(^3P) \rightarrow O_2(a^1\Delta_g) + O(^3P)$ or $O_2(X^3\Sigma_g^-) + O(^3P)$	$2 \cdot 10^{-11} \times \exp(-3700/T)$	this work, see text
------	---	---	------------------------

The quenching of the excited oxygen atoms $O(^1D)$ in collisions with O_2 molecules is an important channel for the excitation of metastable states $O_2(b^1\Sigma_g^+)$ in oxygen plasmas via reaction (R2), see Table 2. This process had been studied well both experimentally [48], [54]–[62] and theoretically [63]. Here we used the value $-4 \cdot 10^{-11} \text{ cm}^3\text{s}^{-1}$ for the total rate constant at 298 K, as recommended in [49], with the temperature dependence described in [48]. The branching ratio between channels (R1) and (R2) was taken from the experimental data of [54], [56], [57], equal 20% and 80% respectively. It should be noted that a significant part of the excitation energy in reaction (R2) goes to $O_2(b^1\Sigma_g^+, v=1)$ state ($\sim 40\%$) [58], [62]. However, we attributed it all to the ground vibrational state $O_2(b^1\Sigma_g^+, v=0)$ due to rapid relaxation of $O_2(b^1\Sigma_g^+, v=1)$ by O_2 molecules [64].

We included reaction (R3) in our new kinetic scheme since it may play an essential role at high gas temperatures. This reaction is the reverse of the $O_2(b^1\Sigma_g^+)$ production process (R2) and its rate constant was obtained from [50] using the calculated thermodynamic equilibrium constant combined with the measured rate of the forward reaction (R2). In addition, the reaction (R4) was taken into account with the temperature dependence $k_{(R4)}(T) = (7.4 \pm 0.8) \cdot 10^{-17} \cdot T^{0.5} \cdot \exp((-1105.7 \pm 53.3)/T) \text{ cm}^3\text{s}^{-1}$ (see Table 2) in accordance with recent data of [51].

The key difference between the present scheme and that presented in [23] is our treatment of the reactions of $O_2(a^1\Delta_g)$ and $O_2(b^1\Sigma_g^+)$ with $O(^3P)$ atoms. In the previous kinetic scheme [23] the quenching of metastable states $O_2(a^1\Delta_g)$ and $O_2(b^1\Sigma_g^+)$ by $O(^3P)$ atoms simply treated by reactions (R5) and (R6) (see Table 2) with rate constants estimated from room-temperature conditions in [65]–[68] for (R5) and in [53] (R6) respectively. Here we will denote these as “collisional quenching” processes. The available literature data on the value rate of the (R5) reaction constant $k_{(R5)}$ range from $1.3 \cdot 10^{-18} \text{ cm}^3\text{s}^{-1}$ to $1 \cdot 10^{-15} \text{ cm}^3\text{s}^{-1}$. In this work, we used the value $-k_{(R5)} = 7 \cdot 10^{-16} \text{ cm}^3\text{s}^{-1}$, recommended in [52]. However, the wide scatter of the available data on $k_{(R5)}$ indicates the need for a more detailed studies on this reaction. The rate constant used for the $O_2(b^1\Sigma_g^+)$ quenching reaction (R6) is $k_{(R6)} = (8 \pm 2) \cdot 10^{-14} \text{ cm}^3\text{s}^{-1}$, which corresponds to the experimental data of [53]. Production of $O_2(a^1\Delta_g)$ in this reaction is faster than the ground state $O_2(X^3\Sigma_g^-)$ due fact that no change of spin is involved. The efficiency of this channel with $O_2(a^1\Delta_g)$ is taken to be 0.75 as recommended in [69].

Additionally, in our previous reaction scheme [23], volume loss of $O_2(a^1\Delta_g)$ was included as via three-body process:



with a rate constant of $-k_{(R5a)} = (1 \div 2.5) \cdot 10^{-32} \text{ cm}^{-6} \text{ s}^{-1}$ with no temperature dependence. The inclusion of reaction (R5a) allowed us to fit the $\text{O}_2(a^1\Delta_g)$ experimental loss rate [3], [23], [47], [70], [71] over a range of gas pressures 7-30 Torr and gas temperatures from 300K up to 750K. The rate constant $k_{(R5a)}$ was estimated from the best agreement between the simulation results and numerous experimental data on the $\text{O}_2(a^1\Delta_g)$ production in discharges for oxygen-iodine lasers [3], [23], [47], [70], [71]. The necessity of introducing reaction (R5a) in [23] was revealed by the fact that the mechanism of fast $\text{O}_2(a^1\Delta_g)$ quenching by vibrationally excited ozone - $\text{O}_3(\text{vib})$, which successfully works in plasma afterglow or photolysis experiments [28], [31], [72], becomes ineffective under the discharge conditions, when the rate of $\text{O}_2(a^1\Delta_g)$ excitation is higher than the $\text{O}_3(\text{vib})$ production rate.

It should be pointed out that previous experiments [3], [23], [47], [70], [71] aimed to maximize the $\text{O}_2(a^1\Delta_g)$ yield, which is vital for discharge oxygen-iodine laser (DOIL). HgO-coating of the tube walls and admixing of small amount of NO for removing $\text{O}(^3\text{P})$ atoms were applied to decrease the $\text{O}_2(a^1\Delta_g)$ volume loss. Therefore the volume quenching of $\text{O}_2(a^1\Delta_g)$ by $\text{O}(^3\text{P})$ was largely suppressed in [3], [23], [47], [70], [71] in comparison with the present experiment. The new experimental data on $\text{O}_2(a^1\Delta_g)$ and $\text{O}_2(b^1\Sigma_g^+)$ concentrations, obtained in the present work over a wide range of gas pressures (10-100 Torr) and (importantly) at higher gas temperatures (700-1700K) reveal a strong temperature dependence of the rates of $\text{O}_2(a^1\Delta_g)$ and $\text{O}_2(b^1\Sigma_g^+)$ volume quenching by $\text{O}(^3\text{P})$ atoms (see next section for details). Therefore we substituted (R5a) reaction by the temperature dependent quenching reaction (R7) for $\text{O}_2(a^1\Delta_g)$. Besides, for generality a new quenching reaction (R8) for $\text{O}_2(b^1\Sigma_g^+)$ was also included:



which we will denote here as a “reactive quenching” processes. Their activation energies, $E_{a1\Delta}$ and $E_{b1\Sigma}$, were estimated by fitting the simulation results to the present experimental data.

All the above considered quenching reactions, (R3), (R5) - (R8), can be understood through the manifold of potential energy surfaces (PES) for the ozone molecule O_3 [73], [74]. Since the quenching of electronic states in these bimolecular reactions is endothermic [52], they will occur mostly through non-adiabatic transitions between different states in the O_3 intermediate [73], [74]. Note that the rate constants for the reactions (R5) and (R6) are rather high compared to quenching on noble gases or molecules like $\text{O}_2(\text{X})$ [45], which also indicates in this favor. In this regard, the separation of the considered reactions into “reactive” and “collisional” quenching were introduced

here for convenience to distinguish reactive channels occurring through a long-lived activated O_3 complex, from collisional quenching (see below).

A correct description of the reaction paths for $O_2(a^1\Delta_g) + O(^3P)$ and $O_2(b^1\Sigma_g^+) + O(^3P)$ over a wide temperature range requires detailed dynamical quantum-mechanical calculations, taking into account a sufficient number of O_3 potential energy surfaces (PES) as well as their non-adiabatic couplings. This is a challenging future task for the quantum chemistry community. Based on the literature on O_3 PES's one can only suppose possible mechanisms for $O_2(a^1\Delta_g)$ and $O_2(b^1\Sigma_g^+)$ reactive quenching by $O(^3P)$ with reasonable activation energy barriers.

An example of PES sections for several O_3 molecular states at fixed lengths of the second O–O bond and bond angle ($\theta = 116.81^\circ$) adapted from [73] are presented in Figure 5. They allow investigation of different possible pathways for reaction (R7). The first involves the creation of a long-lived activated complex, $O_3^*(2^3A'')$, with an energy barrier in the entrance valley of about 0.55 eV. The $2^3A''$ excited state is partially mixed with low-lying electronically excited states ($1^3A''; 1^3A'; 1^1A''$) near the repulsive region of their potentials, due to strong non-adiabatic couplings [74]. This activated complex O_3^* will subsequently decay to form an O_2 molecule in the ground electronic state, since these ozone states ($1^3A''; 1^3A'; 1^1A''$) asymptotically correlate with the $O(^3P) + O_2(X^3\Sigma)$ dissociation limit [74]–[76].

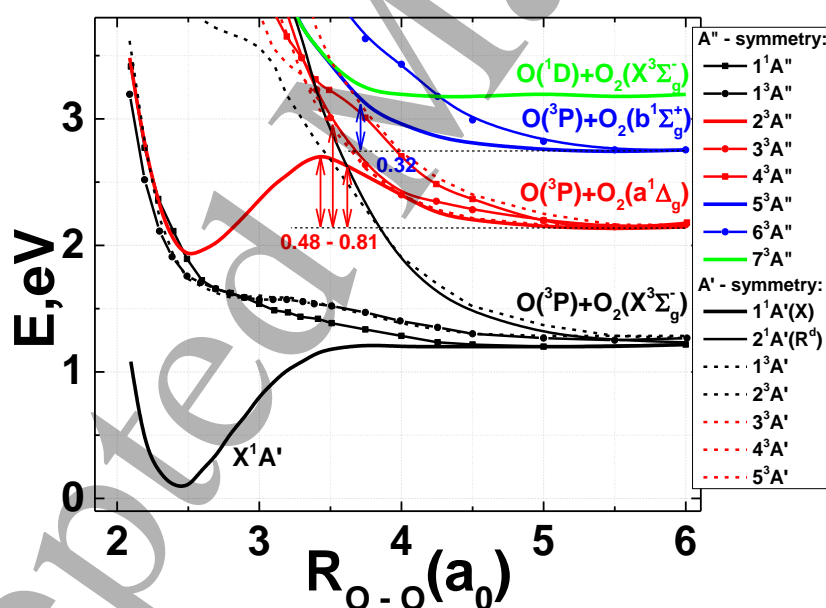


Figure 5. One-dimensional section of ozone molecule PESs along the O–O bond for the lowest three singlet and twelve triplet states in A' and A'' symmetries. The length of the dissociating O–O bond is fixed at $2.4a_0$ and the bond angle is fixed at 116.81° . The adiabatic energies are shown. R^d refers to the diabatic potential curve relevant for dissociation in the Huggins–Hartley band. Adapted from ref. [73]. The possible energy barriers in reactions (R7) and (R8) are shown by red and blue arrows.

The other possible paths for $O_2(a^1\Delta_g)$ quenching are connected with the repulsive character of the $O_2(a^1\Delta_g)$ interaction with $O(^3P)$ over long distances (see Figure 5). The transition from $O_2(a^1\Delta_g) + O(^3P)$ to the $O_2(X^1\Sigma_g^-) + O(^3P)$ system occurs through an area of multiple crossings between several adjacent PESs, allowing non-adiabatic transitions between the PESs [73], [74]. According to Figure 5, the energy barriers for the $O_2(a^1\Delta_g) + O(^3P)$ pathways can vary over a wide range from $\sim 0.48\text{eV}$ to $\sim 0.81\text{eV}$. It should be pointed out that Figure 5 represents only one section of the PESs for the lowest states of O_3 , which is not necessarily a reaction pathway along the reaction coordinate. Determining the exact values of the energy barriers would require detailed quantum-mechanical calculations of the PESs in the vicinities of their intersections for all molecular symmetries, as well as calculations of the minimal energy paths for each corresponding reaction.

Such reaction paths in the repulsive region could compete with a path associated with activated-complex O_3^\pm formation on $2^3A''$ PES. Full clarification of the branching ratio between these channels, and the overall reactivity of $O_2(a^1\Delta_g)$ quenching by $O(^3P)$, would require detailed studies over the whole temperature range. However, note that reactions which occur through spin-forbidden transitions contribute mainly at low gas temperatures, while the “reactive” channel with significant energy barrier become crucial at high T_{gas} [77]. Having this in mind we can validate the “reactive” quenching path - introduced here as reaction (R7) - via our experimental data at $T > 800\text{K}$, while assuming that the rate for the collisional quenching channel is known from the low temperature literature data on (R5). Using this as a first approximation, in our plasma simulations the value for the activation energy barrier value for the reaction (R7) was found to be more than 0.48 eV (see below).

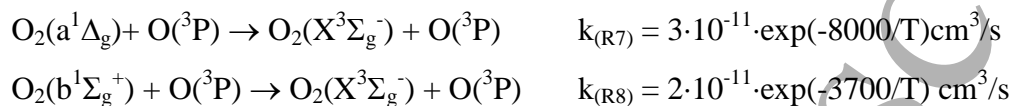
The same considerations can be applied to $O_2(b^1\Sigma_g^+)$ quenching of reaction (R8). As before, this can occur via several complex interactions between different PESs of O_3 excited states, as can be seen from Figure 5. However, the product channel $O(^3P) + O_2(a^1\Delta_g)$ appears more preferable at first glance. Note here that only one section of the PESs is presented. Therefore, this can be considered as assumption. Nevertheless, in a similar way to $O_2(a^1\Delta_g)$, one can expect an energy barrier to reaction (R8). According to Figure 5 this energy barrier should be about 0.32eV . We use this value for temperature dependence of the rate constant of reaction (R8) in our simulations (see next section). Note that a comparable activation energy for the reaction (R8) was also assumed earlier in [78], [79] in the lower temperature range $T_g < 800\text{K}$.

In this work, the proposed mechanisms for the quenching reactions of $O_2(a^1\Delta_g)$ and $O_2(b^1\Sigma_g^+)$ are validated against the experimental data for the temperature range $700\text{K} \leq T_g \leq 1700\text{K}$. In the model we used an Arrhenius form for the rate constant of reaction (R7), $k_{(R7)} = k_{a1\Delta} \exp(-E_{a1\Delta}/T_g)$, where the two parameters, activation energy $E_{a1\Delta}$ and rate constant $k_{a1\Delta}$, were deduced

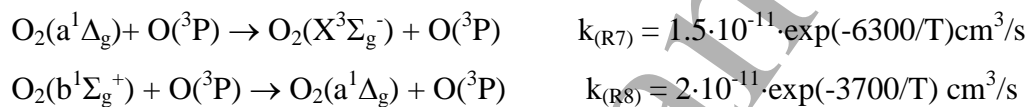
from best fitting of the simulation results to the experimental data on $[\text{O}_2(a^1\Delta_g)]/N$ and $[\text{O}_2(b^1\Sigma_g^+)]/N$. The rate constant for the $\text{O}_2(b^1\Sigma_g^+)$ reactive quenching in reaction (R8) was assumed to behave in the same manner, $k_{(R8)} = k_{b1\Sigma} \exp(-E_{b1\Sigma}/T_g)$. The activation energy $E_{b1\Sigma}$ and the rate constant $k_{b1\Sigma}$ was then obtained in the same way by fitting the simulation results to experimental measurements of $[\text{O}_2(b^1\Sigma_g^+)]/N$ (see next section for details).

While modeling the experimental data we considered two scenarios, since the distribution over the different exit channels in the reaction (R8) is still under discussion:

Scenario A: $\text{O}_2(b^1\Sigma_g^+)$ molecules are assumed to be quenched via reaction (R8) to the ground state, $\text{O}_2(X^3\Sigma_g^-)$:



Scenario B: we assume that quenching reaction (R8) leads to formation of the $\text{O}_2(a^1\Delta_g)$ state:

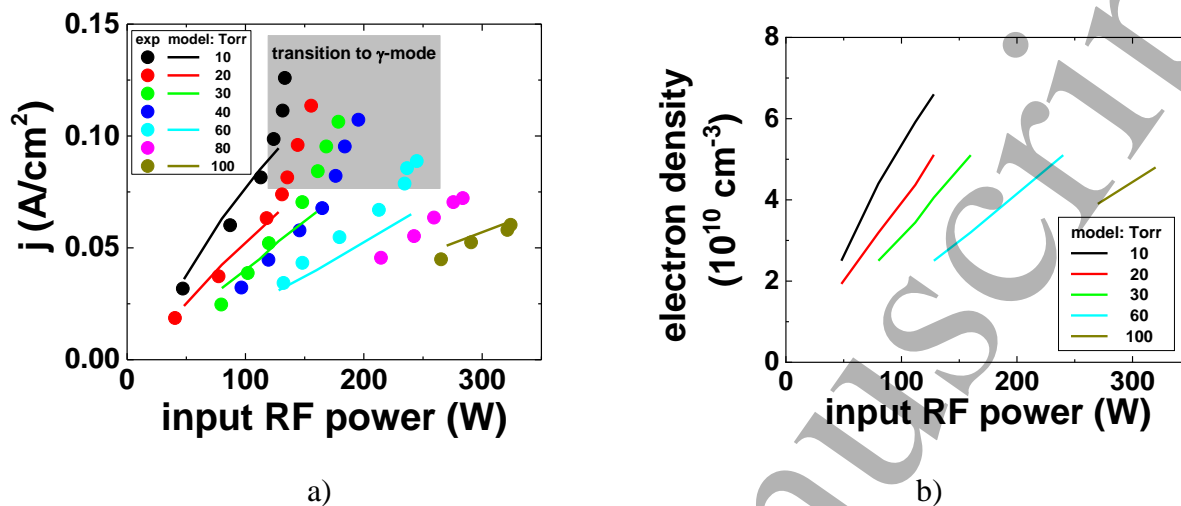


Since in Scenario B the reaction (R8) becomes a significant additional source for $\text{O}_2(a^1\Delta_g)$ production, the temperature dependence $k_{(R7)}(T)$ was corrected as discussed below. The quenching rate constants of $\text{O}_2(a^1\Delta_g)$ and $\text{O}_2(b^1\Sigma_g^+)$ in both scenarios were found from the best fit to experimental data over the whole range of studied conditions.

4. Results and Discussion

Before a detailed discussion on the reactive quenching of $\text{O}_2(a^1\Delta_g)$ and $\text{O}_2(b^1\Sigma_g^+)$ by $\text{O}(^3\text{P})$ atoms, it is important to ensure that the model correctly describes the experiment and reproduces all of the available experimental data, including the electrical discharge characteristics. The jVC (current-voltage) or jPC (current-power) characteristics are fundamental parameters of high-pressure discharge in dielectric tubes, which allow the characterization of the plasma. The current-power characteristics of the discharge are shown in Figure 6a. Dark circles are experimental data, solid lines are model results. The transition from α -mode to γ -mode is clear, indicated by a grey rectangle. Only the α -mode was considered in the model, and therefore data from the γ -mode were excluded from the comparison. As seen, the model reproduces the general trends with rf power and pressure and also the current density values. This agreement of the simulated and experimental jPCs and the reduced electric fields indirectly confirms our description of the electron density [34]. The

calculated electron density as function of input rf power is shown in Figure 6b. It is seen that, for all considered conditions, the electron density, n_e , varies over the limited range $(2-6) \cdot 10^{10} \text{ cm}^{-3}$. We attempted to determine n_e experimentally using the microwave hairpin probe, placing the hairpin antenna on the external side of the tube. Unfortunately in this case the hairpin resonance was very broad, and did not allow accurate measurements of n_e . However, it could provide an estimation of electron density within an accuracy of $(4 \pm 2) \cdot 10^{10} \text{ cm}^{-3}$.



s

Figure 6. a) Discharge current density $j=J_{\text{rf}} \cdot \sin(\Delta\phi)$ as function of rf power dissipated in the plasma. $\Delta\phi$ is the phase shift between the rf voltage and the rf current. The dark circles are experimental data, the solid lines are modeling results. The transition to the γ -mode is shown by a grey rectangle. b) calculated electron density as function of input rf power.

Another important parameter affecting $\text{O}_2(a^1\Delta_g)$ and $\text{O}_2(b^1\Sigma_g^+)$ quenching by $\text{O}(^3\text{P})$ atoms is the gas temperature. The gas temperature $T_{\text{g_axis}}$ in the area close to the tube axis is shown as a function of input rf power in Figure 7. The model results for two values of the temperature near the tube wall $T_{\text{g_w}}$, 400K (solid lines) and 300K (dashed lines) are also presented. The calculated $T_{\text{g_axis}}$ increases by 50-90K with increasing $T_{\text{g_w}}$. The model results with $T_{\text{g_w}}=400\text{K}$ are closer to the measured values of $T_{\text{g_axis}}$, especially at higher gas pressures and rf power inputs. It should be noted that this increase is almost within the scatter of the experimental data. As can be seen in Figure 6, the model results on $T_{\text{g_axis}}$ are generally in good agreement with the measured temperature over the whole range of gas pressures and rf power inputs.

The mole fraction of atomic oxygen, $[\text{O}(^3\text{P})]/N$, as function of input rf power at different pressures is presented in Figure 8. The dark circles represent actinometry data, the lines are model results using the two different values of the gas temperature near the walls (400K (solid lines) and 300K (dashed lines)). As seen from Figure 8, calculated values of $[\text{O}(^3\text{P})]/N$ are in good agreement with the actinometry data over the whole range of discharge parameters under study. At lower pressures of 10-30 Torr, the transition from α -mode to γ -mode is evident from a noticeable change

in the measured $[O(^3P)]/N$ dependence on power input, as discussed above in Figure 6. As seen in Figure 8, the calculated $[O(^3P)]/N$ is somewhat higher at $T_{g,w}=400K$ than at 300K, since the three-body atom recombination rate in reaction $O(^3P)+O(^3P)+O_2 \rightarrow 2O_2$, which causes significant $O(^3P)$ atom loss, decreases with increased T_g due to the temperature-dependent rate constant.

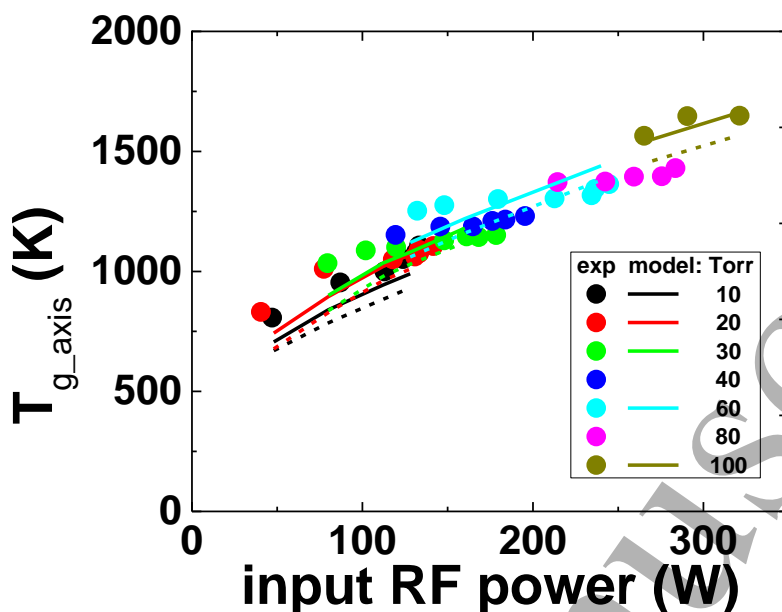


Figure 7. Gas temperature at the tube axis, $T_{g,axis}$, (dark circles are experimental data, lines are simulation results) as a function of the input rf power for all used discharge conditions. The solid lines correspond to assuming $T_{g,w}$ to be 400K in model, and 300K (dashed lines). (see text for details)

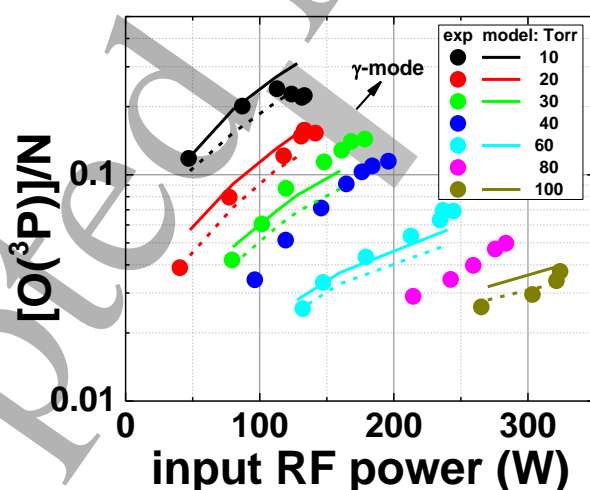


Figure 8. Mole fraction of atomic oxygen, $[O(^3P)]/N$, as function of the input rf power at different pressures. The dark circles are actinometry data, lines are model results assuming the temperature near walls to be 400K (solid lines) and 300K (dashed lines). See text for details.

In this way, the good agreement obtained between the experimental data and the model for the gas temperature and the $[\text{O}(^3\text{P})]/N$ mole fraction allow us to evaluate the rate constants for $\text{O}_2(a^1\Delta_g)$ and $\text{O}_2(b^1\Sigma_g^+)$ reactive quenching by $\text{O}(^3\text{P})$ atoms in reactions (R7) and (R8). It should be also pointed out that the basic characteristics of the discharge, notably j_{PC} , n_e , T_g and $[\text{O}(^3\text{P})]/N$ are hardly affected by the different scenarios for $\text{O}_2(a^1\Delta_g)$ and $\text{O}_2(b^1\Sigma_g^+)$ quenching by $\text{O}(^3\text{P})$ atoms, discussed earlier. This situation allows us to examine the quenching mechanism in more detail.

Experiments using partial modulation (< 20%) of the rf power were performed to investigate the $\text{O}_2(a^1\Delta_g)$ kinetics under active discharge conditions. The plasma parameters equilibrate rapidly during partial modulation (the characteristic time is of the order of a few hundred microseconds, indicated by the Kr and Ar emission intensities [34]). The gas temperature also responds quickly (~3 ms) to small changes in the rf power (as seen in Figure 6). The $\text{O}_2(a^1\Delta_g)$ mole fraction dynamics - $[\text{O}_2(a^1\Delta_g)]/N$, for three pressures 10, 20 and 40 Torr during partial modulation are shown in Figure 9.

The dynamics of the gas density, N , was estimated from the dynamics of the gas temperature using the dependence on rf power shown in Figure 7 and assuming a relaxation time of 3 ms. Any uncertainty connected with this would slightly influence on $[\text{O}_2(a^1\Delta_g)]/N$ dynamics immediately following the power modulation. As seen above, the $\text{O}_2(a^1\Delta_g)$ mole fraction drops as the pressure and the discharge power are increased. It is worth noting that this was observed for all studied discharge conditions. The $\text{O}_2(a^1\Delta_g)$ mole fraction is observed to change in the opposite direction to the power modulation, and the amplitude increases with both pressure and rf power. Only for the lowest input rf power and low pressure do the $\text{O}_2(a^1\Delta_g)$ mole fraction remain almost unchanged.

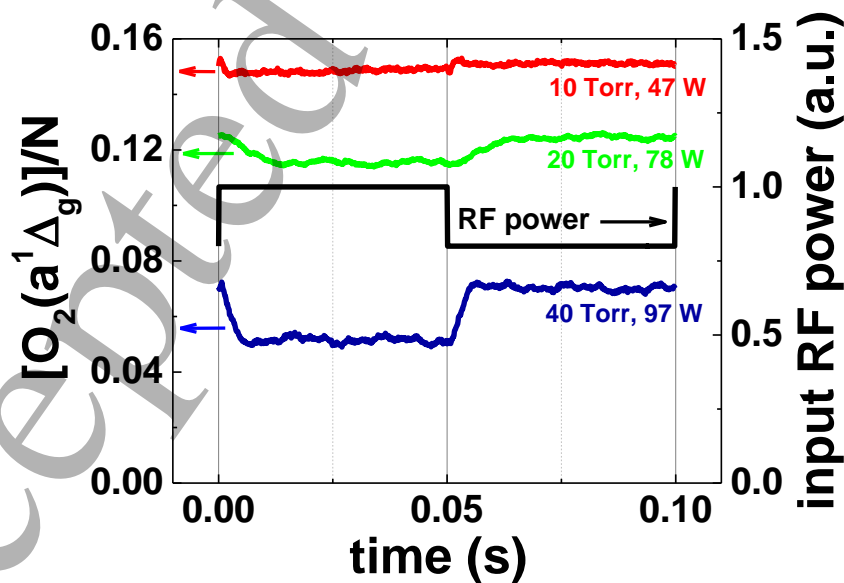


Figure 9. $\text{O}_2(a^1\Delta_g)$ mole fraction dynamics, $[\text{O}_2(a^1\Delta_g)]/N$, during partial (~20%) modulation of the rf power.

The mole-fraction $[O_2(a^1\Delta_g)]/N$ and the absolute density $[O_2(a^1\Delta_g)]$ are shown as a functions of the input rf power for different pressures in Figure 10 a) and b) respectively. The experimental data are presented together with model results. The calculated values for $[O_2(a^1\Delta_g)]/N$ and $[O_2(a^1\Delta_g)]$ were spatially averaged along the inter-electrode distance to compare with experimental data, since the $O_2(a^1\Delta_g)$ and $O_2(b^1\Sigma_g^+)$ emissions were averaged over the tube diameter due to the spectrometer slit. (See Part 2 for details).

The model results in the case of Scenario A, presented in Figure 10, agree well with the experimental data over the whole range of discharge parameters under study. The relative contributions of different $O_2(a^1\Delta_g)$ loss processes are presented in Table 3 for some sets of discharge parameters.

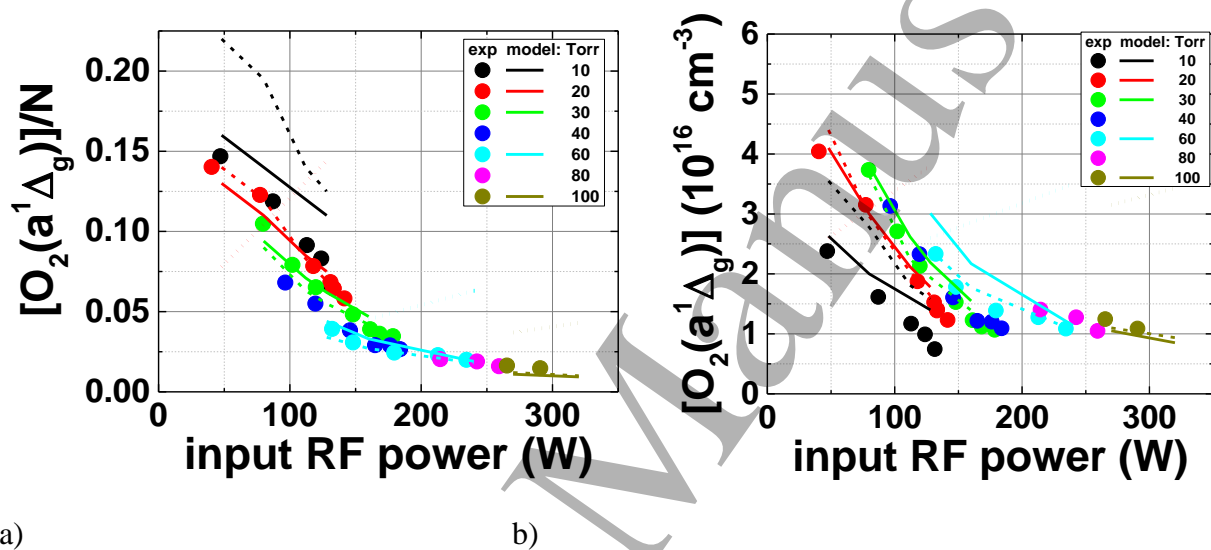


Figure 10. Mole fraction, $[O_2(a^1\Delta_g)]/N$ - (a) and $[O_2(a^1\Delta_g)]$ density - (b) as a function of input rf power for different pressures and $T_{g,w}=400K$. Dark symbols are experimental data, lines are modeling results. Solid and dashed lines correspond to scenarios A and B respectively. The dotted lines correspond to the “old” kinetic scheme without taking into account the reactions (R7) and (R8) (see text for details).

Table 3. Relative contributions from different volume source and loss reactions for $O_2(a^1\Delta_g)$.

Scenario A.

Reaction	10 Torr 48W	10 Torr 128W	30 Torr 80 W	30 Torr 160 W	60 Torr 160W	60 Torr 240W
Source channels						
$O_2+e \rightarrow O_2(a^1\Delta_g)+e$	33%	40%	54%	61%	65%	67%
$O_2^{**}+O_2/O(^3P) \rightarrow O_2(a^1\Delta_g)+O_2/O(^3P)$	11%	11%	18%	18%	23%	23%
$O_2(b^1\Sigma_g^+)+O(^3P) \rightarrow O_2(a^1\Delta_g)+O(^3P)$	53%	42%	27%	19%	11%	10%

Collisional quenching (R6)						
Other reactions	3%	7%	1%	2%	1%	0%
Loss channels						
$O_2(a^1\Delta_g)+e \rightarrow O_2(b^1\Sigma_g^+)+e$	46%	36%	33%	18%	13%	8%
$O_2(a^1\Delta_g)+e \rightarrow O_2+e$	24%	20%	17%	10%	7%	4%
$O_2(a^1\Delta_g)+O(^3P) \rightarrow O_2+O(^3P)$	14%	8%	12%	5%	5%	2%
Collisional quenching (R5)						
$O_2(a^1\Delta_g)+O(^3P) \rightarrow O_2+O(^3P)$	3%	26%	20%	61%	63%	80%
Reactive quenching (R7)						
Other reactions	13%	10%	18%	6%	12%	6%

It is important to note that at gas pressures in the range 10-20 Torr, reactive quenching (R7) only weakly contributes to the $O_2(a^1\Delta_g)$ losses, especially at lower rf power inputs. This is due to the low O atom density and reduced gas temperature. As follows from Table 3, under these conditions the main $O_2(a^1\Delta_g)$ losses are i) electron excitation from $O_2(a^1\Delta_g)$ to $O_2(b^1\Sigma_g^+)$ and ii) secondary electron impact (electron de-excitation to the ground state). This fact is fully confirmed by experimental data on $[O_2(a^1\Delta_g)]/N$ dynamics during partial modulation of the rf power, presented in Figure 9. At the low pressure of 10 Torr and the lowest input rf power of 48W the experimental data on $[O_2(a^1\Delta_g)]/N$ stay almost unchanged during 20% rf power modulation. This can occur only if the $O_2(a^1\Delta_g)$ loss terms are directly proportional to the electron density, in similar way to the $O_2(a^1\Delta_g)$ source term.

Reactive quenching (R7) becomes the dominant process for $O_2(a^1\Delta_g)$ loss as the pressure is increased, whereas the role of quenching by electrons significantly reduces, as follows from Table 3. One can also see that, at moderate pressures of about 30 Torr, the relative role of process (R7) noticeably increases with rf power, due to the simultaneous increases in gas temperature and $O(^3P)$ density.

The model results assuming Scenario B are also presented in Figure 10, along with scenario A for comparison. In case of Scenario B, the reactive quenching of $O_2(b^1\Sigma_g^+)$ to $O_2(a^1\Delta_g)$ in reaction (R8) provides an additional source of $O_2(a^1\Delta_g)$. This source becomes more significant at low gas pressures, because the $O_2(b^1\Sigma_g^+)$ density increases significantly as the pressure is decreased - see Figure 11. As a result, the rate constant (R7) for Scenario B needs to be slightly higher to fit the observations, compared to Scenario A. This further requires a reduction of the energy threshold to 6300 K from 8000K. Even using these adjustments, the modelled $[O_2(a^1\Delta_g)]/N$ and $[O_2(a^1\Delta_g)]$ values at 10 Torr are still about 30% higher than in Scenario A. This is because the additional source of $O_2(a^1\Delta_g)$ in reaction (R8) in Scenario B is maximal at low pressure, whereas the effect of $O_2(a^1\Delta_g)$ reactive quenching in (R7) is small, as illustrated in Table 3 and Figure 9. This is due to

the relatively low gas temperature and $O(^3P)$ atom concentration, as discussed above. Nevertheless, the error in our absolute calibration is estimated to be of the same order ($\sim 30\%$) whereas the error in relative emission measurements is $\sim 10\%$. As a result, it is currently difficult to decide between the two scenarios. As seen in Figure 9, they both provide reasonable agreement to the existing experimental data.

For comparison, the results of simulations using the previous kinetic scheme [1] are also presented in Figure 10 for 20, 60 and 100 Torr. The old scheme includes a 3-body mechanism for $O_2(a^1\Delta_g)$ quenching - (R5a) with a temperature-independent rate coefficient, in the place of the reactive quenching process (R7). As can be seen, simulations using reaction (R5a) are able to predict the observed pressure trends up to 60 Torr. However, they also predict a rise of the $[O_2(a^1\Delta_g)]/N$ mole-fraction and the $[O_2(a^1\Delta_g)]$ density with rf power. This substantially contradicts the experimental trend. In contrast, calculations including the reactive quenching process (R7), with either scenario A or B, are in good agreement with the observations. This is further confirmation of the existence of a reactive quenching process (R7) which exponentially increases with gas temperature.

The $O_2(b^1\Sigma_g^+)$ mole fraction, $[O_2(b^1\Sigma_g^+)]/N$, is shown in Figure 11 as a function of rf power for different pressures, along with the model results for scenarios A and B. As can be seen, the two scenarios have little effect on the modelled $[O_2(b^1\Sigma_g^+)]/N$, since the rate constant $k_{(R8)} = 2 \cdot 10^{11} \cdot \exp(-3700/T) \text{ cm}^3/\text{s}$, is the same in both cases.

The relative contributions of different production and loss channels for $O_2(b^1\Sigma_g^+)$ are presented in Table 4 for several sets of discharge parameters. The main production channel of $O_2(b^1\Sigma_g^+)$ is reaction (R2), while $O(^1D)$ atoms are produced directly from O_2 dissociation and by electron impact excitation of O atoms. As for the loss channels, reactive quenching (R8) is the main loss process for $O_2(b^1\Sigma_g^+)$ over the whole range of conditions studied. However, at low gas pressures (10-20 Torr) and low rf power, quenching of $O_2(b^1\Sigma_g^+)$ by $O(^3P)$ atoms by (R6) also makes a notable contribution to the total loss rate.

In addition to comparing the spatially averaged $O_2(a^1\Delta_g)$ densities and the mole fractions ($O_2(a^1\Delta_g)/N$, $O_2(b^1\Sigma_g^+)/N$ and $O(^3P)/N$), it is useful to consider also their calculated spatial distribution. The key reactive quenching reactions, (R7) and (R8), strongly depend on gas temperature, which is not spatially uniform, and neither are the densities of neutral species. As a result, the reaction rates will vary across the tube in a complex fashion. Although the actual discharge geometry is complex, the 1D model can provide qualitative understanding of these spatial effects.

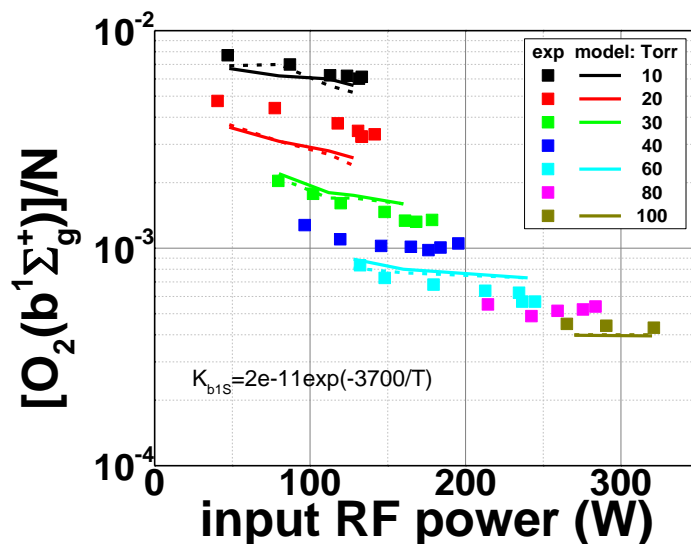


Figure 11. $O_2(b^1\Sigma_g^+)$ mole fraction, $[O_2(b^1\Sigma_g^+)]/N$, as a function of input rf power for different pressures and $T_{g,w}=400K$. Dark squares are experimental data, lines are the simulations. Solid and dashed lines correspond to scenario A and B respectively (see text for details).

Table 4. Relative contributions from different volume source and loss reactions for $O_2(b^1\Sigma_g^+)$.

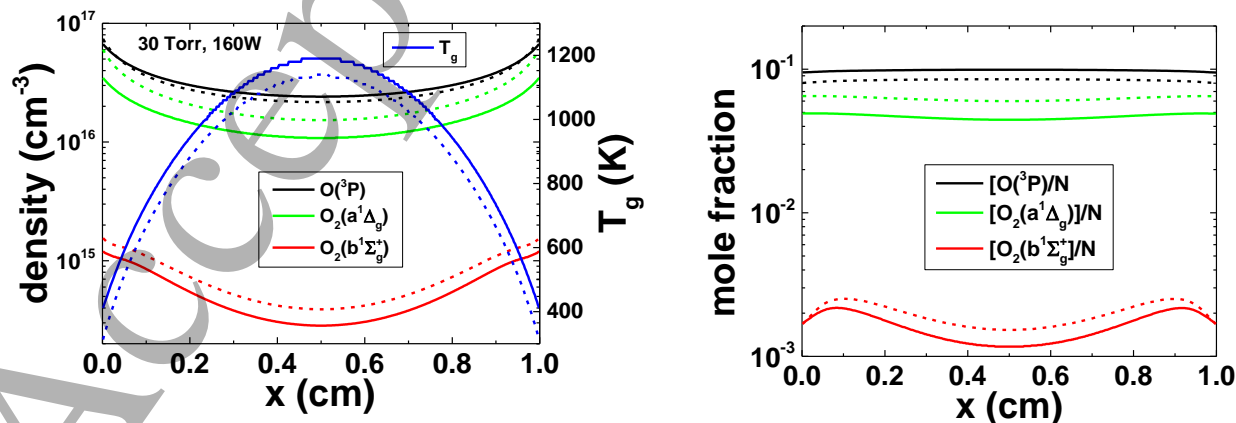
Scenario A.

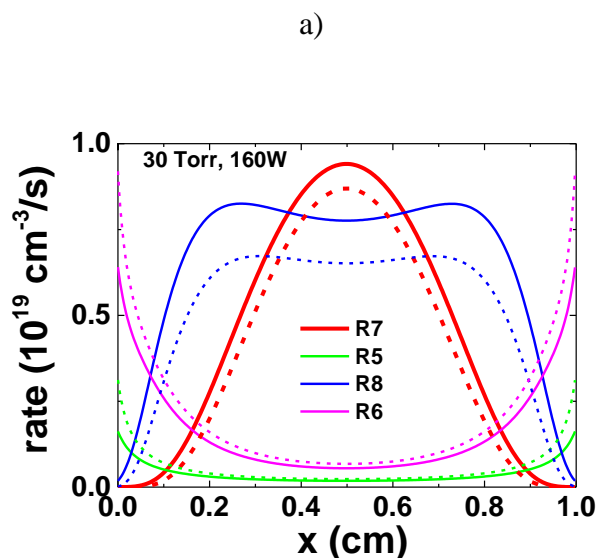
Reaction	10 Torr 48W	10 Torr 128W	30 Torr 80 W	30 Torr 160 W	60 Torr 160W	60 Torr 240W
Source channels						
$O_2(a^1\Delta_g)+e \rightarrow O_2(b^1\Sigma_g^+)+e$	35%	25%	33%	14%	14%	9%
$O_2+e \rightarrow O_2(b^1\Sigma_g^+)+e$	9%	8%	21%	19%	30%	28%
$O_2+O(^1D) \leftrightarrow O_2(b^1\Sigma_g^+)+O(^3P)$ (R2)- (R3)	51%	64%	35%	58%	41%	49%
Other reactions	5%	3%	11%	9%	15%	14%
Loss channels						
$O_2(b^1\Sigma_g^+)+O(^3P) \rightarrow O_2(a^1\Delta_g)+O(^3P)$	55%	31%	34%	21%	16%	14%
Collisional quenching (R6)						
$O_2(b^1\Sigma_g^+)+O(^3P) \rightarrow O_2+O(^3P)$ Reactive quenching (R8)	38%	65%	57%	72%	68%	76%
Other reactions	7%	4%	9%	7%	16%	10%

Figure 12a presents calculated spatial transverse profiles of the $O_2(a^1\Delta_g)$, $O_2(b^1\Sigma_g^+)$ and $O(^3P)$ absolute densities, as well as the spatial distributions of the gas temperature for a pressure of 30 Torr and input rf power of 160W. The concave distributions of $O_2(a^1\Delta_g)$ and $O(^3P)$ densities, showing a minimum in the center, reflects the spatial distribution of the gas temperature and the resultant minimum in the total gas density in the center of the tube. In contrast, the spatial

distribution of the mole fractions $O_2(a^1\Delta_g)/N$ and $O(^3P)/N$ presented in Figure 12b are almost uniform. The spatial distribution of the $O_2(b^1\Sigma_g^+)$ density is more complex, although it also has a minimum in the center. The mole-fraction, $O_2(b^1\Sigma_g^+)/N$, is not uniform but dips in the center, due to the high volume loss frequency for $O_2(b^1\Sigma_g^+)$ compared to $O_2(a^1\Delta_g)$ and $O(^3P)$.

In order to understand the effect of the gas temperature near the wall, $T_{g,w}$, dashed lines in Figure 12a and 12b indicate the spatial distribution of the same species and the gas temperature with the gas temperature near the wall set to $T_{g,w}=300K$. The influence of $T_{g,w}$ parameter on the axial gas temperature and the $O(^3P)$ atom mole fraction was already discussed earlier (see Figure 7 and 8). As for the $O_2(a^1\Delta_g)$ and $O_2(b^1\Sigma_g^+)$ densities, they are about 1.5-2 times higher at $T_{g,w}=300K$ than at 400K. This difference is much greater than can be explained simply by the change in T_g , but must instead be caused by the decrease in reactive quenching rates (R7) and (R8) with decreasing gas temperature. This is confirmed by Figure 12c, where spatial distributions of the different reaction rates, $R = kN_aN_b$, are presented for both cases $T_{g,w}=300K$ than at 400K. As is seen, the rates of both reactions (R7) and (R8) are reduced as the gas temperature decreases, whereas the temperature-independent reaction rates of (R5) and (R6) increase, due to the increase in $O_2(a^1\Delta_g)$ and $O_2(b^1\Sigma_g^+)$ densities. The rates of reactions (R5) and (R6) have concave profiles, similar to the spatial distributions of the related species $O_2(a^1\Delta_g)$, $O_2(b^1\Sigma_g^+)$ and $O(^3P)$. At the same time the rate of (R7) has a strongly convex shape that reflects mostly the gas temperature profile which has an exponential dependence on T_g , despite the concave profiles of $O_2(a^1\Delta_g)$ and $O(^3P)$. Thus $O_2(a^1\Delta_g)$ molecules are destroyed efficiently in the center of the tube, where the gas temperature is maximal. The distribution of the rate of reaction (R8) is more complex, as it depends on both the exponential dependence of the reaction rate on T_g and concave profile of the $O_2(b^1\Sigma_g^+)$ density. In addition, the spatial profile of the rate of (R8) is wider than for (R7) (see in Figure 12) due to its lower activation energy compared to (R7). Based on the above analysis, it should be pointed out once more, that even small uncertainties in $T_{g,w}$ and the resultant ~ 50 -100K change in T_g would lead to a visible change in the calculated values for the $O_2(a^1\Delta_g)$ and $O_2(b^1\Sigma_g^+)$ densities, and also add some uncertainty in our estimations of the rate constants for (R7) and (R8).





c)

Figure 12. Calculated spatial profiles of $O_2(a^1\Delta_g)$, $O_2(b^1\Sigma_g^+)$, $O(^3P)$ densities and gas temperature (a) and mole fractions (b); and spatial distributions of reaction rates (R5)-(R8), rate = $k[Na][Nb]$ (c) for the Scenario A (see the text). The solid lines are the results for $T_{g_w} = 400K$, and dashed lines for $T_{g_w} = 300K$.

The resultant temperature dependences for the rate constants of the reactive quenching reactions, (R7) and (R8), are shown in Figure 13 for the both scenarios A and B. Quite good agreement is seen between the experimental and simulation for the $O_2(a^1\Delta_g)$ density over a wide range of conditions ($P = 20-100Torr$ and $T_g = 800-1700K$), for conditions where process (R7) dominates $O_2(a^1\Delta_g)$ loss, allowing us to validate the rate constant $k_{(R7)}$ with quite good accuracy. The uncertainty in the value of $k_{(R7)}$ is associated with the uncertainties in the products of reaction (R8), which may follow scenarios A or B – see Figure 13.

Note that the mechanism of $O_2(a^1\Delta_g)$ reactive quenching by $O(^3P)$ atoms – (R7), which was proposed here for the first time and validated against an experimental dataset over a wide range of discharge conditions, plays a crucial role. It significantly increases the quenching of $O_2(a^1\Delta_g)$ at temperatures above $\sim 800K$ compared to the commonly used collisional quenching reaction (R5) (see Table 3 and Figure 13).

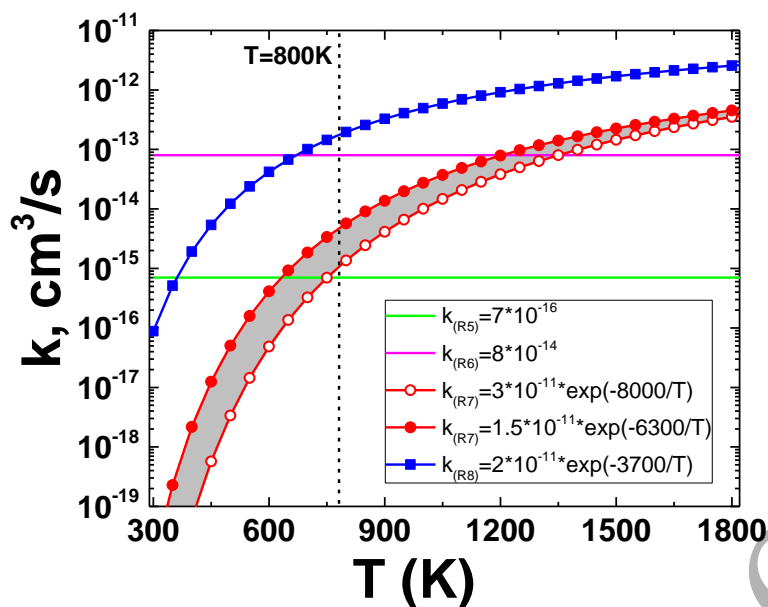


Figure 13. Temperature dependencies for the rate constants of $O_2(a^1\Delta_g)$ reactive quenching in reaction (R7) for both scenarios A and B. The same rate constant for reactive quenching of $O_2(b^1\Sigma_g^+)$ in reaction (R8) was used in both scenarios. The horizontal lines are the rate constants of “collisional” quenching of $O_2(a^1\Delta_g)$ in (R5) and $O_2(b^1\Sigma_g^+)$ in (R6). The grey area between two (R7) rate constants used in scenarios A and B indicates possible uncertainty in $k_{(R7)}$ value. A vertical dashed line at $T=800K$ indicates an approximate boundary, where $O_2(a^1\Delta_g)$ reactive quenching in (R7) starts to play a crucial role (see the text).

5. Conclusion

Fast quenching of $O_2(a^1\Delta_g)$ by $O(^3P)$ atoms at high temperature was experimentally observed at the first time. The experiments were carried out in an 81MHz CCP discharge in oxygen at pressures of 10-100Torr in a quartz tube with external electrodes to provide high power input, i.e. both high temperature and significant $O(^3P)$ density simultaneously. It was observed that the rate of $O_2(a^1\Delta_g)$ quenching by $O(^3P)$ atoms rises rapidly with gas temperature above $\sim 800K$.

Possible mechanisms of $O_2(a^1\Delta_g)$ quenching by $O(^3P)$ atoms were considered, based on analysis of available PESs for the O_3 molecule, and were consistent with the presence of a high activation energy barrier in reactive channel $O_2(a^1\Delta_g) + O(^3P)$. This mechanism was included in an updated scheme of kinetic processes in O_2 plasma. The experimental results were interpreted with the aid of a self-consistent 1D model of the CCP discharge. This model showed that only the inclusion of a temperature-activated channel for $O_2(a^1\Delta_g)$ quenching by atomic oxygen allows the experimental data to be reproduced. Without this channel the model even predicts some trends in opposition the experimental observations.

A comprehensive consideration of the relative contributions of different loss processes for $O_2(a^1\Delta_g)$ in the model showed that at lower gas pressures (10-20 Torr) this reactive quenching only makes a weak contribution, and is dominated by electron impact processes (excitation from $O_2(a^1\Delta_g)$ to $O_2(b^1\Sigma_g^+)$ and secondary electron impact). At pressures above 20 Torr reactive quenching progressively dominates the $O_2(a^1\Delta_g)$ loss, especially at higher rf power input due to the simultaneous increase in gas temperature and $O(^3P)$ density. The excellent agreement of the model with the experimental measurements of the $O_2(a^1\Delta_g)$ density allowed us to determine the rate constant of $O_2(a^1\Delta_g)$ quenching on $O(^3P)$ atoms with good accuracy, giving a value within the range $3 \cdot 10^{-11} \times \exp(-8000/T)$ cm^3/s to $1.5 \cdot 10^{-11} \times \exp(-6300/T)$ cm^3/s over a wide range of discharge conditions ($P = 20\text{-}100\text{Torr}$ and $T_g = 800\text{-}1700\text{K}$).

Comparison of the experimental results for $O_2(b^1\Sigma_g^+)$ to the model also showed that an analogous reactive quenching process occurs for $O_2(b^1\Sigma_g^+)$ molecules. Only by including in the model a fast $O_2(b^1\Sigma_g^+)$ quenching reaction by atomic oxygen, with activation energy about of ~ 3700 K, were we able to explain the measured low concentrations of $O_2(b^1\Sigma_g^+)$ and its variations with discharge parameters. Best fitting of the simulation results to the $[O_2(b^1\Sigma_g^+)]/N$ data provided a rate constant of $2 \cdot 10^{-11} \cdot \exp(-3700/T)$ cm^3/s . This observed quenching of $O_2(a^1\Delta_g)$ and $O_2(b^1\Sigma_g^+)$ by oxygen atoms has a significant impact on the dynamics of oxygen plasmas, and is likely to play a major impact on the kinetics of oxygen-containing discharge mixtures at higher gas temperatures, for example in plasma-assisted combustion or in high-pressure plasma processing reactors.

Acknowledgements

This research was conducted in the scope of the KAPPA International Associated Laboratory (LIA) and supported by Russian Foundation for Basic Research (RFBR) Grants No. 16-52-16024 and 18-32-00932.

ORCID iDs

A V Volynets <https://orcid.org/0000-0003-4893-764>

D V Lopaev <https://orcid.org/0000-0003-4975-3487>

A A Chukalovsky <https://orcid.org/0000-0003-3556-3252>

T V Rakhimova <https://orcid.org/0000-0003-3539-4823>

O V Proshina

J P Booth <https://orcid.org/0000-0002-0980-3278>

References

- [1] D. B. Graves, "The emerging role of reactive oxygen and nitrogen species in redox biology and some implications for plasma applications to medicine and biology," *J. Phys. D. Appl. Phys.*, vol. 45, no. 26, p. 263001, Jul. 2012, doi: 10.1088/0022-3727/45/26/263001.
- [2] I. Adamovich *et al.*, "The 2017 Plasma Roadmap: Low temperature plasma science and technology," *J. Phys. D. Appl. Phys.*, vol. 50, no. 32, p. 323001, Aug. 2017, doi: 10.1088/1361-6463/aa76f5.
- [3] O. V Braginsky *et al.*, "Pressure scaling of an electro-discharge singlet oxygen generator (ED SOG)," *J. Phys. D. Appl. Phys.*, vol. 40, no. 21, pp. 6571–6582, Nov. 2007, doi: 10.1088/0022-3727/40/21/017.
- [4] A. A. Ionin, I. V Kochetov, A. P. Napartovich, and N. N. Yuryshev, "Physics and engineering of singlet delta oxygen production in low-temperature plasma," *J. Phys. D Appl. Phys.*, vol. 40, no. 2, pp. R25–R61, Jan. 2007, doi: 10.1088/0022-3727/40/2/R01.
- [5] D. L. Carroll *et al.*, "Enhanced performance of an electric oxygen-iodine laser," *Proc. SPIE*, vol. 7581, pp. 758102-758102–8, Feb. 2010, doi: 10.1117/12.845913.
- [6] A. Hicks *et al.*, "Design and operation of a supersonic flow cavity for a non-self-sustained electric discharge pumped oxygen-iodine laser," *J. Phys. D. Appl. Phys.*, vol. 40, no. 5, pp. 1408–1415, Mar. 2007, doi: 10.1088/0022-3727/40/5/014.
- [7] M. C. Heaven, "Recent advances in the development of discharge-pumped oxygen-iodine lasers," *Laser Photon. Rev.*, vol. 4, no. 5, pp. 671–683, Sep. 2010, doi: 10.1002/lpor.200900052.
- [8] V. N. Azyazov, A. P. Torbin, A. A. Pershin, P. A. Mikheyev, and M. C. Heaven, "Kinetics of oxygen species in an electrically driven singlet oxygen generator," *Chem. Phys.*, vol. 463, pp. 65–69, Dec. 2015, doi: 10.1016/j.chemphys.2015.09.007.
- [9] A. A. Konnov, "Role of excited species in hydrogen combustion," *Combust. Flame*, vol. 162, no. 10, pp. 3755–3772, 2015.
- [10] A. M. Starik, B. I. Loukhovitski, A. S. Sharipov, and N. S. Titova, "Physics and chemistry of the influence of excited molecules on combustion enhancement," *Philos. Trans. R. Soc. A*, vol. 373, p. 20140341, 2015.
- [11] A. A. Chukalovsky *et al.*, "Study of Singlet Delta Oxygen O₂(¹Δ_g) Impact on H₂-O₂ Mixture Ignition in Flow Reactor: 2D Modeling," *Combust. Sci. Technol.*, vol. 184, no. 10–11, pp. 1768–1786, Oct. 2012, doi: 10.1080/00102202.2012.690980.
- [12] T. Ombrello, S. H. Won, Y. Ju, and S. Williams, "Flame propagation enhancement by plasma excitation of oxygen. Part II: Effects of O₂(a¹Δ_g)," *Combust. Flame*, vol. 157, no. 10, pp. 1916–1928, Oct. 2010, doi: 10.1016/j.combustflame.2010.02.004.
- [13] A. V. Lebedev, M. A. Deminsky, A. V. Zaitzevsky, and B. V. Potapkin, "Effect of O₂(a¹D_g)

on the low-temperature mechanism of CH₄ oxidation,” *Combust. Flame*, vol. 160, no. 3, pp. 530–538, Mar. 2013, doi: 10.1016/j.combustflame.2012.11.020.

- [14] J. P. Booth *et al.*, “Oxygen (3 P) atom recombination on a Pyrex surface in an O₂ plasma,” *Plasma Sources Sci. Technol.*, vol. 28, no. 5, p. 055005, May 2019, doi: 10.1088/1361-6595/ab13e8.
- [15] O. V Braginsky *et al.*, “Pressure scaling of an electro-discharge singlet oxygen generator (ED SOG),” *J. Phys. D. Appl. Phys.*, vol. 40, no. 21, pp. 6571–6582, Nov. 2007, doi: 10.1088/0022-3727/40/21/017.
- [16] O. V Braginsky *et al.*, “High pressure electro-discharge singlet oxygen generator (ED SOG) with high efficiency and yield,” *J. Phys. D. Appl. Phys.*, vol. 41, no. 17, p. 172008, Sep. 2008, doi: 10.1088/0022-3727/41/17/172008.
- [17] B. S. Woodard *et al.*, “The influence of radio-frequency discharge geometry on O₂ (a 1 Δ) production,” *J. Phys. D. Appl. Phys.*, vol. 44, no. 11, p. 115102, Mar. 2011, doi: 10.1088/0022-3727/44/11/115102.
- [18] C. Lee, D. B. Graves, M. A. Lieberman, and D. W. Hess, “Global Model of Plasma Chemistry in a High Density Oxygen Discharge,” *J. Electrochem. Soc.*, vol. 141, no. 6, p. 1546, 1994, doi: 10.1149/1.2054960.
- [19] V. V. Ivanov, K. S. Klopovsky, D. V. Lopaev, a. T. Rakhimov, and T. V. Rakhimova, “Experimental and theoretical investigation of oxygen glow discharge structure at low pressures,” *IEEE Trans. Plasma Sci.*, vol. 27, no. 5, pp. 1279–1287, 1999, doi: 10.1109/27.799804.
- [20] S. G. Belostotsky, D. J. Economou, D. V Lopaev, and T. V Rakhimova, “Negative ion destruction by O(3 P) atoms and O₂ (a 1 Δ g) molecules in an oxygen plasma,” *Plasma Sources Sci. Technol.*, vol. 14, no. 3, pp. 532–542, Aug. 2005, doi: 10.1088/0963-0252/14/3/016.
- [21] A. Annušová *et al.*, “Kinetics of highly vibrationally excited O₂ (X) molecules in inductively-coupled oxygen plasmas,” *Plasma Sources Sci. Technol.*, vol. 27, no. 4, p. 045006, Apr. 2018, doi: 10.1088/1361-6595/aab47d.
- [22] A. N. Vasiljeva *et al.*, “On the possibility of O₂(a1Dg) production by a non-self-sustained discharge for oxygen–iodine laser pumping,” *J. Phys. D. Appl. Phys.*, vol. 37, no. 17, pp. 2455–2468, Sep. 2004, doi: 10.1088/0022-3727/37/17/019.
- [23] O. V Braginskiy *et al.*, “Singlet oxygen generation in O₂ flow excited by RF discharge: I. Homogeneous discharge mode: α-mode,” *J. Phys. D. Appl. Phys.*, vol. 38, no. 19, pp. 3609–3625, Oct. 2005, doi: 10.1088/0022-3727/38/19/010.
- [24] H. Hannesdottir and J. T. Gudmundsson, “On singlet metastable states, ion flux and ion energy in single and dual frequency capacitively coupled oxygen discharges,” *J. Phys. D.*

Appl. Phys., vol. 50, no. 17, p. 175201, May 2017, doi: 10.1088/1361-6463/aa65ed.

- [25] G. Gousset *et al.*, “Electron and heavy-particle kinetics in the low pressure oxygen positive column,” *J. Phys. D. Appl. Phys.*, vol. 24, no. 3, pp. 290–300, Mar. 1991, doi: 10.1088/0022-3727/24/3/010.
- [26] I. A. Kossyi, A. Y. Kostinsky, A. A. Matveyev, and V. P. Silakov, “Kinetic scheme of the non-equilibrium discharge in nitrogen-oxygen mixtures,” *Plasma Sources Sci. Technol.*, vol. 1, no. 3, pp. 207–220, Aug. 1992, doi: 10.1088/0963-0252/1/3/011.
- [27] D. S. Stafford and M. J. Kushner, “O₂(Δ₁) production in He/O₂ mixtures in flowing low pressure plasmas,” *J. Appl. Phys.*, vol. 96, no. 5, pp. 2451–2465, Sep. 2004, doi: 10.1063/1.1768615.
- [28] R. T. V. Klopovskii K.S., Kovalev A.S., Lopaev D.V., Rakhimov A.T., “The Role of Vibrationally Excited Ozone in the Formation of Singlet Oxygen in a Oxygen-Nitrogen Plasma,” *Sov.J. Plasma Phys. (USA)*, vol. 18, no. 12, pp. 834–839, 1992.
- [29] A. D. Palla *et al.*, “Oxygen discharge and post-discharge kinetics experiments and modeling for the electric oxygen-iodine laser system,” *J. Phys. Chem. A*, vol. 111, no. 29, pp. 6713–21, Jul. 2007, doi: 10.1021/jp069003+.
- [30] V. N. Azyazov, P. Mikheyev, D. Postell, and M. C. Heaven, “O₂(a₁Δ) quenching in the O/O₂/O₃ system,” *Chem. Phys. Lett.*, vol. 482, no. 1–3, pp. 56–61, Nov. 2009, doi: 10.1016/j.cplett.2009.09.095.
- [31] K. S. Klopovskii, A. S. Kovalev, D. V Lopaev, N. A. Popov, and A. T. Rakhimov, “New mechanism of singlet-oxygen production in processes with participation of electronically and vibrationally excited ozone molecules,” *J. Exp. Theor. Phys.*, vol. 80, no. April, pp. 603–613, 1995.
- [32] J. G. J. Steinfeld, S. Adler-Golden, “Critical Survey of Data on the Spectroscopy and Kinetics of Ozone in the Mesosphere and Thermosphere,” *J. Phys. Chem. Ref. Data*, vol. 16, no. 4, pp. 911–951, 1987.
- [33] Y. V Savin *et al.*, “Singlet oxygen production and quenching mechanisms in travelling microwave discharges,” *J. Phys. D. Appl. Phys.*, vol. 37, no. 22, pp. 3121–3128, Nov. 2004, doi: 10.1088/0022-3727/37/22/010.
- [34] A. V Volynets, D. V Lopaev, S. M. Zyryanov, M. A. Bogdanova, and A. T. Rakhimov, “Volume and surface loss of O(3 P) atoms in O₂ RF discharge in quartz tube at intermediate pressures (10–100 Torr),” *J. Phys. D. Appl. Phys.*, vol. 52, no. 39, p. 395203, Sep. 2019, doi: 10.1088/1361-6463/ab28dc.
- [35] S. M. Zyryanov and D. V. Lopaev, “Measurements of the gas temperature in an oxygen plasma by spectroscopy of the O₂(b₁Σ_g⁺) → O₂(X₃Σ_g⁻) transition,” *Plasma Phys. Reports*, vol. 33, no. 6, pp. 510–520, 2007, doi: 10.1134/S1063780X07060086.

- [36] D. A. Newnham and J. Ballard, "Visible absorption cross sections and integrated absorption intensities of molecular oxygen (O_2 and O_4)," *J. Geophys. Res. Atmos.*, vol. 103, no. D22, pp. 28801–28815, Nov. 1998, doi: 10.1029/98JD02799.
- [37] S. S. Tayal and O. Zatsarinny, "B-spline R-matrix-with-pseudostates approach for excitation and ionization of atomic oxygen by electron collisions," *Phys. Rev. A*, vol. 94, no. 4, p. 042707, Oct. 2016, doi: 10.1103/PhysRevA.94.042707.
- [38] R. R. Laher and F. R. Gilmore, "Updated Excitation and Ionization Cross Sections for Electron Impact on Atomic Oxygen," *J. Phys. Chem. Ref. Data*, vol. 19, no. 1, pp. 277–305, Jan. 1990, doi: 10.1063/1.555872.
- [39] J. E. Chilton, J. B. Boffard, R. S. Schappe, and C. C. Lin, "Measurement of electron-impact excitation into the $3p^5 4p$ levels of argon using Fourier-transform spectroscopy," *Phys. Rev. A*, vol. 57, no. 1, pp. 267–277, Jan. 1998, doi: 10.1103/PhysRevA.57.267.
- [40] J. E. Chilton, M. D. Stewart, and C. C. Lin, "Cross sections for electron-impact excitation of Krypton," *Phys. Rev. A*, vol. 62, no. 3, p. 032714, Aug. 2000, doi: 10.1103/PhysRevA.62.032714.
- [41] G. J. M. Hagelaar and L. C. Pitchford, "Solving the Boltzmann equation to obtain electron transport coefficients and rate coefficients for fluid models," *Plasma Sources Sci. Technol.*, vol. 14, no. 4, pp. 722–733, Nov. 2005, doi: 10.1088/0963-0252/14/4/011.
- [42] A. Kramida, Y. Ralchenko, J. Reader, and N. A. Team, "NIST Atomic Spectra Database (ver. 5.3), [Online]," *National Institute of Standards and Technology, Gaithersburg, MD*, 2018. .
- [43] K. S. Klopovskiy, D. V. Lopaev, N. A. Popov, A. T. Rakhimov, and T. V. Rakhimova, "Heterogeneous quenching of $O_2(1\Delta_g)$ molecules in $H_2 : O_2$ mixtures," *J. Phys. D Appl. Phys.*, vol. 32, pp. 3004–3012, 1999.
- [44] P. Borrell, P. M. Borrell, and M. D. Pedley, "Deactivation of singlet molecular oxygen, $O_2(1\Delta_g)$, by oxygen," *Chem. Phys. Lett.*, vol. 51, no. 2, pp. 300–302, Oct. 1977, doi: 10.1016/0009-2614(77)80407-7.
- [45] A. Leiss, U. Schurath, K. H. Becker, and E. H. Fink, "Revised quenching rate constants for metastable oxygen molecules $O_2(a^1\Delta_g)$," *J. Photochem.*, vol. 8, no. 2, pp. 211–214, Jan. 1978, doi: 10.1016/0047-2670(78)80021-5.
- [46] K. Tachibana and A. V. Phelps, "Excitation of the $O_2(a^1\Delta_g)$ state by low energy electrons," *J. Chem. Phys.*, vol. 75, no. 7, pp. 3315–3320, Oct. 1981, doi: 10.1063/1.442483.
- [47] O. V. Proshina *et al.*, "Discharge singlet oxygen generator for oxygen–iodine laser: II. Two-dimensional modelling of flow oxygen rf plasma at 13.56 and 81 MHz power frequency," *J. Phys. D. Appl. Phys.*, vol. 39, no. 24, pp. 5191–5200, Dec. 2006, doi: 10.1088/0022-3727/39/24/015.

- [48] G. E. Streit, C. J. Howard, A. L. Schmeltekopf, J. A. Davidson, and H. I. Schiff, "Temperature dependence of O(¹D) rate constants for reactions with O₂, N₂, CO₂, O₃, and H₂O," *J. Chem. Phys.*, vol. 65, no. 11, pp. 4761–4764, Dec. 1976, doi: 10.1063/1.432930.
- [49] W. B. DeMore *et al.*, "Chemical Kinetics and Photochemical Data for Use in Stratospheric Modeling," Pasadena, 1997. [Online]. Available: https://jpldataeval.jpl.nasa.gov/pdf/Atmos97_Anotated.pdf.
- [50] R. B. J. ZINN, C. D. SUTHERLAND, S. N. STONE, L. M. DUNCAN, "Ionospheric effects of rocket exhaust products-HEAO-C, Skylab," *J. Atmos. Terr. Phys.*, vol. 44, no. 12, pp. 1143–1171, 1982.
- [51] M. V. Zagidullin *et al.*, "O₂ (b¹Σ_g⁺) quenching by O₂, CO₂, H₂O, and N₂ at temperatures of 300-800K," *J. Phys. Chem. A*, 2017, doi: 10.1021/acs.jpca.7b07885.
- [52] A. N. Dvoryankin, L. B. Ibragimov, Y. A. Kulagin, and L. A. Shelepin, "Plasma Chemistry, ed. BM Smirnov," *Energoatomizdat, Moscow*, vol. 14, p. 102, 1987.
- [53] T. G. Slanger and G. Black, "Interactions of O₂ (b¹Σ_g⁺) with O(³P) and O₃," *J. Chem. Phys.*, vol. 70, no. 7, pp. 3434–3438, Apr. 1979, doi: 10.1063/1.437877.
- [54] L. C. Lee and T. G. Slanger, "Atmospheric OH production—The O(¹D) + H₂O reaction rate," *Geophys. Res. Lett.*, vol. 6, no. 3, pp. 165–166, Mar. 1979, doi: 10.1029/GL006i003p00165.
- [55] R. A. Young and G. Black, "Deactivation of O(¹D)," *J. Chem. Phys.*, vol. 47, no. 7, pp. 2311–2318, Oct. 1967, doi: 10.1063/1.1703312.
- [56] P. H. Wine and A. R. Ravishankara, "Kinetics of O(1D) interactions with the atmospheric gases N₂, N₂O, H₂O, H₂, CO₂, and O₃," *Chem. Phys. Lett.*, vol. 77, no. 1, pp. 103–109, Jan. 1981, doi: 10.1016/0009-2614(81)85609-6.
- [57] J. Shi and J. R. Barker, "Kinetic studies of the deactivation of O₂(1Σ_g⁺) and O(1D)," *Int. J. Chem. Kinet.*, vol. 22, no. 12, pp. 1283–1301, Dec. 1990, doi: 10.1002/kin.550221207.
- [58] J. G. Green, J. Shi, and J. R. Barker, "Photochemical Kinetics of Vibrationally Excited Ozone Produced in the 248 nm Photolysis of O₂/O₃ Mixtures," *J. Phys. Chem. A*, vol. 104, no. 26, pp. 6218–6226, Jul. 2000, doi: 10.1021/jp000635k.
- [59] N. Taniguchi, K. Hirai, K. Takahashi, and Y. Matsumi, "Relaxation Processes of Translationally Hot O(1D) by Collisions with O₂," *J. Phys. Chem. A*, vol. 104, no. 17, pp. 3894–3899, May 2000, doi: 10.1021/jp994291d.
- [60] K. Takahashi, Y. Takeuchi, and Y. Matsumi, "Rate constants of the O(1D) reactions with N₂, O₂, N₂O, and H₂O at 295 K," *Chem. Phys. Lett.*, vol. 410, no. 4–6, pp. 196–200, Jul. 2005, doi: 10.1016/J.CPLETT.2005.05.062.
- [61] R. Grondin, J.-C. Loison, and K. M. Hickson, "Low Temperature Rate Constants for the

Reactions of O(1D) with N₂, O₂, and Ar,” *J. Phys. Chem. A*, vol. 120, no. 27, pp. 4838–4844, Jul. 2016, doi: 10.1021/acs.jpca.5b12358.

- [62] L. C. Lee and T. G. Slanger, “Observations on O(1D→3P) and O₂(b 1Σ_g⁺ →X 3Σ_g⁻) following O₂ photodissociation,” *J. Chem. Phys.*, vol. 69, no. 9, p. 4053, 1978, doi: 10.1063/1.437136.
- [63] N. Miura, K. Hashimoto, K. Takahashi, N. Taniguchi, and Y. Matsumi, “Electronic quenching of O(1D) by collisions with O₂: A theoretical study in a collinear case,” *J. Chem. Phys.*, vol. 116, no. 13, pp. 5551–5556, Apr. 2002, doi: 10.1063/1.1457433.
- [64] A. S. Kirillov, “Model of the vibrational level population of the b 1Σ_g⁺ state of oxygen molecules at heights of the lower thermosphere and mesosphere,” *Geomagn. Aeron.*, vol. 52, no. 3, pp. 383–389, May 2012, doi: 10.1134/S0016793212030085.
- [65] R. P. Wayne, “Singlet molecular oxygen,” *Adv. Photochem.*, vol. 7, no. 3, p. 1, 1969.
- [66] M. J. McEwan and L. F. Phillips, *Chemistry of the Atmosphere (Christchurch, New Zealand: University of Canterbury)*. New York, 1975.
- [67] W. F. J. Evans, D. M. Hunten, E. J. Llewellyn, and A. V. Jones, “Altitude profile of the infrared atmospheric system of oxygen in the dayglow,” *J. Geophys. Res.*, vol. 73, no. 9, pp. 2885–2896, May 1968, doi: 10.1029/JA073i009p02885.
- [68] D. M. Hunten, “Spectroscopic studies of the twilight airglow,” *Space Sci. Rev.*, vol. 6, no. 4, pp. 493–573, 1967, doi: 10.1007/BF00173704.
- [69] R. Atkinson *et al.*, “Evaluated Kinetic, Photochemical and Heterogeneous Data for Atmospheric Chemistry: Supplement V. IUPAC Subcommittee on Gas Kinetic Data Evaluation for Atmospheric Chemistry,” *J. Phys. Chem. Ref. Data*, vol. 26, no. 3, pp. 521–1011, May 1997, doi: 10.1063/1.556011.
- [70] O. V Braginskiy *et al.*, “Singlet oxygen generation in O₂ flow excited by RF discharge: II. Inhomogeneous discharge mode: plasma jet,” *J. Phys. D. Appl. Phys.*, vol. 38, no. 19, pp. 3626–3634, Oct. 2005, doi: 10.1088/0022-3727/38/19/011.
- [71] O. V Braginsky *et al.*, “Discharge singlet oxygen generator for oxygen–iodine laser: I. Experiments with rf discharges at 13.56 and 81 MHz,” *J. Phys. D. Appl. Phys.*, vol. 39, no. 24, pp. 5183–5190, Dec. 2006, doi: 10.1088/0022-3727/39/24/014.
- [72] V. N. Azyazov, P. A. Mikheyev, and M. C. Heaven, “On the O₂ (a 1 Δ) quenching by vibrationally excited ozone,” vol. 2, no. 1.
- [73] H. Zhu, Z.-W. Qu, M. Tashiro, and R. Schinke, “On spin-forbidden processes in the ultra-violet photodissociation of ozone,” *Chem. Phys. Lett.*, vol. 384, no. 1–3, pp. 45–51, Jan. 2004, doi: 10.1016/j.cplett.2003.11.095.
- [74] S. Y. Grebenshchikov, Z.-W. Qu, H. Zhu, and R. Schinke, “New theoretical investigations of the photodissociation of ozone in the Hartley, Huggins, Chappuis, and Wulf bands,” *Phys.*

Chem. Chem. Phys., vol. 9, no. 17, p. 2044, 2007, doi: 10.1039/b701020f.

- 1
2
3
4
5
6
7
8
9
10
11
12
13
14
15
16
17
18
19
20
21
22
23
24
25
26
27
28
29
30
31
32
33
34
35
36
37
38
39
40
41
42
43
44
45
46
47
48
49
50
51
52
53
54
55
56
57
58
59
60
- [75] R. Dawes, P. Lolur, A. Li, B. Jiang, and H. Guo, “Communication: An accurate global potential energy surface for the ground electronic state of ozone,” *J. Chem. Phys.*, vol. 139, no. 20, p. 201103, 2013, doi: 10.1063/1.4837175.
- [76] S. Y. Grebenshchikov, Z.-W. Qu, H. Zhu, and R. Schinke, “Spin-orbit mechanism of predissociation in the Wulf band of ozone,” *J. Chem. Phys.*, vol. 125, no. 2, p. 021102, Jul. 2006, doi: 10.1063/1.2219444.
- [77] J. N. Harvey, “Understanding the kinetics of spin-forbidden chemical reactions,” *Phys. Chem. Chem. Phys.*, vol. 9, no. 3, pp. 331–343, 2007, doi: 10.1039/B614390C.
- [78] J. P. Booth *et al.*, “Density of metastable O₂(b¹Σ_g⁺) molecules in an O₂/DC discharge measured by vacuum ultraviolet absorption and optical emission spectroscopy,” in *The 71st Annual Gaseous Electronics Conference, Co-Located with the 60th Annual meeting of the APS Division of Plasma Physics*, 2018, p. GT1.049, [Online]. Available: <https://ui.adsabs.harvard.edu/abs/2018APS..GECGT1049B/abstract>.
- [79] J.-P. Booth *et al.*, “A comprehensive diagnostic study of a DC positive column in O₂: a test-bed for models of plasmas in a diatomic gas,” in *Frontiers in low Temperature plasma simulation*, 2019, [Online]. Available: <https://tel.archives-ouvertes.fr/X-LPTP/hal-02341779v1>.